Department of Physics and Astronomy
Heidelberg University

Master Thesis in Physics
submitted by

Simon Groß-Bölting

born in Heidelberg (Germany)

December 2024

Material Budget Imaging for mockup samples of the ALICE ITS3 with an electron beam at energies of 2.4 GeV and 4.8 GeV

This Master Thesis has been carried out by Simon Groß-Bölting at the
Physikalisches Institut of the University of Heidelberg
under the supervision of
Prof. Dr. Silvia Masciocchi

Abstract

In the upcoming Long Shutdown 3, the ALICE experiment will replace the inner barrel of its current ITS2 detector with the ITS3. The ITS3 features curved, wafer-scale, ultra-thin silicon sensors held in place by ultra-light carbon foam support structures. By combining six of these sensors and attaching the support structure only to the sensor edges, the ITS3 aims to achieve an unprecedented average material budget. For the first layer, the material budget within $|\eta| < 1$ is expected to average 0.09 %.

To investigate the scattering introduced by the carbon foam support structures, a mockup of the ITS3 was constructed. Using an electron scattering telescope optimized for angular resolution, the scattering angles of electrons on targets were measured, and distributions were created based on the interpolated positions of the scattered electrons.

The scattering angle distribution width was extracted by fitting the inner 98 % of the distribution with a Gaussian. The material budget was then inferred using the Highland formula, after applying quadratic subtraction, non-linearity corrections and using position-based momentum calculations derived from scattering on calibration targets. This approach produced a two-dimensional material budget map. Notably, the position-based momentum correction enhanced accuracy by accounting for momentum gradients in the test beam and eliminated the need for a scaling factor.

The measured material budget for the "half-ring" was found to align with theoretical predictions, while deviations in the "longeron" were attributed to excess glue, as confirmed by CT scans.

Zusammenfassung

Im kommenden Long Shutdown 3 wird im ALICE Experiment der innere Teil ("inner barrel" genannt) des ITS2 Detektors durch den ITS3 ersetzt. Der ITS3 besteht aus sechs Wafergroßen, extrem dünnen, gebogenen Siliziumsensoren, die von ultaleichten Kohlenstoffschaum-Trägerstruckturen gehalten werden. Da die Trägerstrucktur nur an den Sensorkanten befestigt wird, gelingt es mit dem ITS3 ein bislang unerreichtes Materialbudget zu erreichen. Für die innerste Schicht wird innerhalb von $|\eta| < 1$ ein durchschnittliches Materialbudget von 0.09 % erwartet.

Um die Streuung durch die Kohlenstoffschaum-Trägerstrukturen zu untersuchen, wurde ein Mockup-Modell des ITS3 hergestellt. Mit einem für die Winkelauflösung optimierten Elektronenstreuteleskops wurden die Streuwinkel von Elektronen an Targets gemessen, und Streuwinkelverteilungen wurden basierend auf den interpolierten Positionen der gestreuten Elektronen erstellt.

Die Breite der Streuwinkelverteilung wurde durch das Fitten der inneren 98 % mit einer Gaußfunktion extrahiert. Das Materialbudget wurde anschließend mithilfe der Highland-Formel bestimmt, nachdem quadratische Subtraktion, Nichtlinearitätskorrekturen und positionsbasierte Impulsberechnungen aus der Streuung an Kalibrationstargets, angewendet wurden. Mit diesem Verfahren konnten zweidimensionale Materialbudgetkarten erstellt werden. Besonders die positionsbasierte Impulsberechnung verbesserte die Genauigkeit der Materialbudgetmessung, indem sie den im Teststrahl vorkommenden Impulsgradienten berücksichtigt und auch den Bedarf eines Skalierungsfaktors eliminierten.

Das gemessene Materialbudget des "Half-Ring" entsprach den theoretischen Vorhersagen, während Abweichungen beim "Longeron" auf überschüssigen Kleber zurückgeführt wurden, was durch CT-Scans bestätigt werden konnte.

Table of Contents

1 Introduction

The field of research of particle physics aims to study, describe and understand the fundamental particles that make up our Universe and the fundamental forces governing their interactions. Until now the most established theory describing these fundamental forces is the Standard Model of particle physics (SM), which describes three of the four known fundamental forces in the Universe: electromagnetic, weak, and strong interactions, while not covering gravity. It classifies all known particles into fermions and bosons. Fermions, the matter constituents, include quarks and leptons, each organized into three generations distinguished by increasing mass. Quarks carry color charge and interact via the strong force, forming mesons, like pions, and hadrons such as protons and neutrons. Leptons include electrons and neutrinos, for which only electrons participate in both electromagnetic and weak interactions, whereas neutrinos interact solely via the weak force. Bosons are the force carriers: photons mediate the electromagnetic force, W and Z bosons mediate the weak force, and gluons mediate the strong force between quarks. The Higgs boson plays a key role in mass generation through spontaneous symmetry breaking, giving the W and Z bosons, as well as fermions, their mass via interactions with the Higgs field [1]. To verify the existence of the Higgs boson the Large Hadron Collider (LHC) at the European Council for Nuclear Research (CERN), near Geneva in Switzerland, was build. It is the world's largest and most powerful particle accelerator, designed to study collisions between protons with energies of up to $\sqrt{s} = 13.6\,\text{TeV}$ and heavy ions of up to $\sqrt{s_{\text{NN}}} = 5.36\,\text{TeV}$ [2].

One of the experiments located at Interaction Point 2 of the LHC is the "A Large Ion Collider Experiment" (ALICE) which is dedicated to heavy-ion physics. ALICE is designed to study the physics of strongly interacting matter, described by Quantum Chromodynamics (QCD), at the highest energy densities and temperatures reached in a laboratory so far. In such extreme conditions a state of matter, called the Quark–Gluon Plasma (QGP), is formed after the collision, which is also thought to have been the state of matter for the first few µs after the Big Bang [3].

To investigate the properties of the QGP particles emerging from the collision need to be measured and identified. In this process it is not only relevant to measure the energy of those particles but a crucial part is the measurement of their trajectory. The trajectory of a particle not only gives insight on the momentum of the particle via the curvature in the constant magnetic field of 0.5 T in ALICE, but also on the position where those particles originated from or where some decayed into their daughter particles. Those vertices are essential when it comes to reconstructing the events accurately. Higher accuracies on the vertices lead to

more reliable measurements of particle lifetimes, decay modes, and the physical processes which occur after the collisions. Therefore highly accurate measurements of the trajectory and the origin of these particles are needed. In ALICE a variety of different detector systems are used to accomplish this task (see Chapter 2), but they all have in common to scatter the measured particles as little as possible to achieve the best tracking resolution. This can be done by reducing the material of a detector as much as possible to decrease the inference with the particles trajectory. The reduction of material is taken to another level with the new upgrade in the next Long Shutdown (LS) 3 in 2028 of the innermost three layers of the Inner Tracking System (ITS) from its current state the ITS2 to the ITS3 . The current average material budget of the inner layers of the ITS2 with $x/X_0 = 0.35\,\%$ [4] per layer will be decreased with the ITS3 to $x/X_0 = 0.09\,\%$ [5] per layer. The ITS3 will consist of cylindrically shaped, wafer-scale silicon sensors, which are held in place by structural carbon foam pieces which are glued between adjacent sensors.

Until now, the material budget of the ITS3 has only been estimated through theoretical calculations, relying on assumptions about the radiation lengths of the carbon foam and glue, as detailed material properties are often proprietary. For example, manufacturers typically provide density ranges rather than precise radiation length values, making direct calculations challenging. To address this, the carbon foam—a morphological structure of vitreous carbon [5]—is treated as an equivalent block of solid carbon in material budget estimations. However, this assumption may oversimplify its properties, as structural variations, such as glue seeping into the foam, could significantly affect the material budget.

It is crucial to know the material budget of each part of the detector as precise as possible, as the knowledge of the detectors material is used in performing Monte Carlo (MC) simulations and particle tracking. MC simulations play a crucial role in modern experimental physics, serving multiple applications across various stages of data analysis and detector operation. Firstly, they are essential for validation and calibration, allowing for direct comparisons between recorded experimental data and simulated data to verify the performance and reliability of the detectors [6]. Additionally, MC simulations are frequently used to generate synthetic datasets that are employed in training machine learning (ML) models. These models help in distinguishing signal from background, and enhancing candidate and event selection processes [7]. Furthermore, MC simulations are integral to event selection, helping to develop and optimize both online and offline triggers. By predicting the expected detector response for specific event signatures, these simulations guide the tuning of triggers, enabling efficient data reduction in the face of immense data flow [8]. Beyond

these applications, MC simulations are a fundamental tool for comparing theoretical models with experimental results. They accurately replicate particle behavior and detector response based on comprehensive models. The closer the detector models in the MC simulations are to the real-world conditions, the more reliable the comparison between simulated predictions and observed physical phenomena becomes. This highlights the importance of precise knowledge about the material budget, as this ensure that the simulation accurately reflects the actual material composition and structure of the detector, directly influencing the validity of the physical models.

The detector layout and material budget models are also critical components in particle tracking algorithms. Accurate models are necessary for predicting the effects of multiple scattering, energy loss, and deflections caused by the detector materials. Trajectory reconstruction methods, such as those based on the Kalman filter, rely heavily on these models to correctly anticipate the deflections introduced by material in the particle's path [9]. If the material budget is inaccurately modeled, the tracking algorithm may misinterpret the trajectory, leading to incorrect particle identification and, ultimately, the wrong interpretation of the underlying physics. This underscores the importance of precise material budget measurements to ensure reliable tracking performance and trustworthy physics analyses.

Therefore, a measurement is needed to verify the material budget and radiation lengths of the materials used before the detector setup is installed. While photon conversion or hadronic interaction vertices can later map the material in a detector very precisely, such methods require significant photon interaction, which is challenging for ultralight designs with minimal material. To do so, the scattering of electrons on a ITS3 mockup sample is used to infer from the scattering angle distribution the material budget. This method has been shown to be useful [10; 11] and will be further adapted and improved throughout this thesis.

1.1 Coulomb scattering

When a charged particle, such as an electron, interacts with a nucleus it will loose energy and scatters on the electric field of the nucleus. The electromagnetic interaction between those two charged particles is governed by Coulomb's law, which states that the force both experience is:

$$F = \frac{k \cdot q \cdot Q}{r^2}, \tag{1}$$

with q and Q being the charges of both particles, r their distance between each other and k being the Coulomb constant. As a result of this interaction the particle experiences a deflection, changing its trajectory. This deflection can be described by the scattering angle ϕ between the original incoming path and its new outgoing path. The differential cross-section for Coulomb scattering can be described by the Rutherford scattering formula: [12]:

$$\frac{\mathrm{d}\sigma}{\mathrm{d}\Omega} = \frac{1}{4}\left(\frac{q \cdot Q}{4\pi\epsilon_0 E_{kin}}\right)^2 \cdot \frac{1}{\sin^4(\phi/2)}. \tag{2}$$

It expresses the probability, also known as cross section, of a charged particle with charge q scattering at a particular angle ϕ off of a charged target with charge Q. ϵ_0 is the vacuum permittivity and E_{kin} the initial kinetic energy of the incoming particle. For small angles it can be approximated as:

$$\frac{\mathrm{d}\sigma}{\mathrm{d}\Omega} \sim \frac{1}{\phi^4}, \tag{3}$$

which shows, that it is more likely to have small scattering angles with the mean value being zero.

1.2 Multiple Coulomb scattering

When a particle passes through any material due to the increased number of potential scattering partners it will undergo a series of those small-angle Coulomb scattering deflections. This cumulative effect is known as Multiple Coulomb Scattering (MCS). This leads to a collective angular deflection and displacement of the particle from its original path. An illustration of multiple Coulomb scattering process, projected along y, can be seen in Figure 1.1. The particle will scatter in all three dimensions, but the scattering angle that is obtained in the end (θ_{space}) can be projected in x- and y-direction ($\theta_{space} = \sqrt{\theta^2_{plane,X} + \theta^2_{plane,Y}}$), with X and Y being orthogonal to each other and orthogonal to Z which is in the direction of motion of the particle. Throughout this thesis only the planar angles will be used as $\theta_X = \theta_{plane,X}$ and $\theta_Y = \theta_{plane,Y}$.

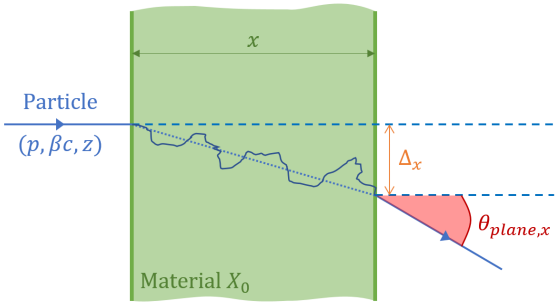

Figure 1.1: Illustration of multiple scattering of a particle (p, z) in material (x, X_0), projected along y.

1.3 Radiation length

The radiation length X_0 is a fundamental property specific to each material. It is defined as the mean distance in a material after which a high-energy electron ($E > 10\,\mathrm{MeV}$) losses all but $1/e$ of its initial energy, which corresponds to an energy loss of about $1 - 1/e \approx 63\,\%$. It loses this energy via bremsstrahlung, which is emitted due to the electron being accelerated and deflected by the field of the atomic nuclei of the material it traverses. The radiation length of a given type of material consisting only of a isotope pure nucleus with atomic number Z and atomic mass A can be approximated with the empirical formula:

$$\rho \cdot X_0 = 716.4\mathrm{g\,cm^{-2}} \cdot \frac{A}{Z(Z+1)\ln\left(\frac{287}{\sqrt{Z}}\right)}. \tag{4}$$

This formula expresses the density ρ of the material and its radiation length in $\mathrm{g\,cm^{-2}}$. By dividing this quantity by the density the radiation length is expressed as a unit of length. For materials with high atomic numbers (like lead), the radiation length is shorter, meaning that particles lose energy and scatter relative to its path more often. In contrast, for lighter materials (like carbon or silicon), the radiation length is longer, resulting in less frequent interactions relative to the path. There are also direct measurements of the radiation length tabulated by the *Particle Data Group*, which will be used in this thesis [13] (Chapter 3.2). To calculate the total radiation length of a composite material, which is a mixture of different type nuclei, the approximation can be used [13]:

$$\frac{1}{X_0} = \sum \frac{w_i}{X_{0,i}}, \tag{5}$$

which is the sum over the weighted w_i radiation lengths of the different contributors $X_{0,i}$, with the weights being the relative fractions of each material contributing.

1.4 Material budget

The material budget is defined as the thickness of the material x in terms of a fraction of the radiation length of that material X_0 as x/X_0. To find the material budget of a composite of materials, formula (5) can be re-written in terms of the material budget to be:

$$\frac{x}{X_0} = \sum_i \frac{x_i}{X_{0,i}}, \tag{6}$$

with x_i being the thickness of the individual materials and x being the thickness of the resulting composite. Therefore the weights can also be expressed as a fraction of the individual thicknesses and the resulting thickness $w_i = x_i/x$. With Gaussian error propagation the

uncertainty on the thicknesses $\sigma(x_i)$ and on the radiation lengths $\sigma(X_{0,i})$ can be propagated such that the error on the material budget comes to be:

$$\sigma\left(\frac{x}{X_0}\right) = \sqrt{\sum_i \left(\frac{\sigma(x_i)}{X_{0,i}}\right)^2 + \left(\frac{x_i \cdot \sigma(X_{0,i})}{X_{0,i}^2}\right)^2}. \tag{7}$$

1.5 Highland formula

Figure 1.2 shows the scattering angle distributions for the $\theta_X = \theta_{plane,X}$ for two different targets, air (blue) and 165 µm of nickel (red). The distributions consists of an inner Gaussian core and infrequent single scattering events with large deflection angles. It can be seen that with increasing material budget also the width of the distribution increases. The theoretical basis for describing MCS was first developed by Molière in the 1940s [14]. Molière's theory provides a comprehensive statistical description of multiple scattering, accounting for both small-angle and large-angle deflections. It considers the interactions as a series of deflections that result in a distribution of scattering angles for a particle passing through a given material. Molière's theory introduced the concept of the characteristic angle θ_0 , which defines the width of the angular distribution due to multiple scattering. For small angles, the distribution follows a Gaussian form due to the central limit theorem, which states that the distribution of a large number of independent, random variables tends towards a normal Gaussian distribution. At larger angles the distribution has non-Gaussian tails due to less frequent single scattering events. The Gaussian nature of the small-angle scattering is crucial for practical applications, as it allows for simplified calculations of the angular deflection.

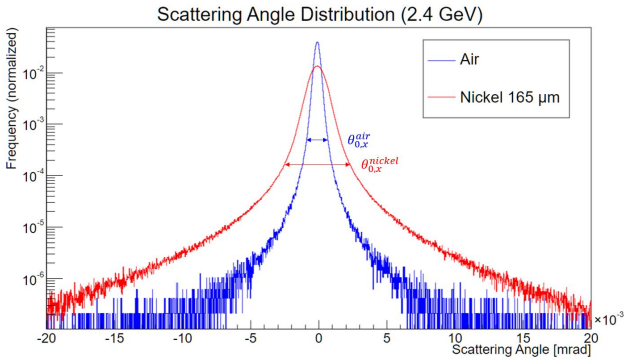

Figure 1.2: Scattering angle distribution measured at 2.4 GeV after traversing air (blue) and 165 µm nickel (red).

A simplification of the full description of Molière's theory is given by the Highland formula, introduced in the 70s by Highland [15], which is an empirical approximation that simplifies the characteristics of the angular distribution of MCS. It relates the scattering angle θ_0 to the material budget x/X_0 of the scattering material. Lynch and Dahl later in the 90s refined the formula even further [16] using the width of a Gaussian when taking the inner 98 % of

the scattering distribution, resulting in the now known *Highland formula* [13]:

$$\theta_0 = \frac{13.6\,\mathrm{MeV}}{\beta cp} q \cdot \sqrt{\frac{x}{X_0}} \left[1 + 0.038 \ln \left(\frac{x}{X_0} \cdot \frac{q^2}{\beta^2} \right) \right], \tag{8}$$

where p is the momentum of the incoming particle, β the particle velocity and q the charge of the incident particle. The formula describes the width of the scattering angle distribution based on the material budget of a scatterer, and by numerical inversion the material budget for a measured scattering angle distribution can be calculated. When multiple of those scattering angle distributions are created based on the positional information the material budget can be inferred and mapped, creating a two dimensional material budget distribution. This procedure is known as **M**aterial **B**udget **I**maging (MBI) and is the basis of this thesis.

2 A Large Ion Collider Experiment

The ALICE experiment is made up of many different sub detectors and a schematic of the entire detector system is shown in Figure 2.1. The so-called central barrel is located inside of the large, red L3 solenoid magnet which generates a $B = 0.5\,\mathrm{T}$ homogeneous magnetic field parallel to the beam line. Charged particles traversing that field will experience an electromagnetic force and according to Lorentz force law their trajectory will be bent when they have a momentum component transverse to the magnetic field:

$$\vec{F} = q\left(\vec{v} \times \vec{B}\right) \quad \text{and} \quad \vec{p}_T = q\left(\vec{B} \times \vec{R}\right) \tag{9}$$

This bending radius $\vec{R}$ is used to determine the transverse momentum $\vec{p}_T$ of the particle, and particles with less momentum will bent more then particles with higher momentum.

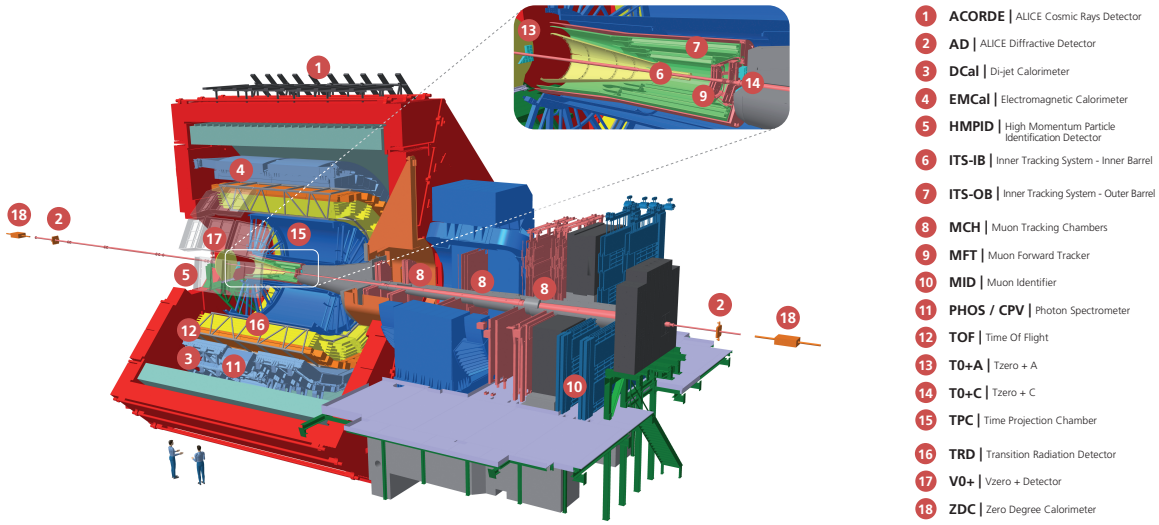

Figure 2.1: Schematic view of the ALICE experiment during Run 3 [17].

The collision point of the highly energetic hadrons is located in the middle of the big red magnet in Figure 2.1. Particles emerge in all directions from this point, and to maximize detection efficiency, the detectors are symmetrically arranged around the beam pipe in a barrel-like structure, ensuring high coverage. To evaluate the trajectories of the particles coming out of the collision multiple detector systems work hand-in-hand and combine their tracking and Particle Identification (PID) information. Focusing only on the few detectors most important in the scope of this thesis. The innermost detector is the Inner Tracking System (ITS), comprised of an Inner Barrel (IB) 6 and Outer Barrel (OB) 7 in Figure 2.1. It is an essential element for the ALICE physics program. It is used for tracking and the

precise measurement of primary and secondary vertices and needs to have a high detection efficiency, high spatial resolution and is highly granular to cope with the high multiplicity that ALICE desires [5]. Further out is the Time Projection Chamber (TPC) 15 which is delivering many measurement points for momentum determination and performs PID via the energy-loss over a given distance for each particle. The tracking information of the TPC is combined with that of the ITS to increase the precision on the vertexing and improve the momentum resolution due to the lever arm. Other detectors offer complementary information and extend the measurement range of the full system.

With the upgrade of ALICE in the LS2 also its readout rate increased from below 1 kHz to 50 kHz in Pb–Pb collisions, leading to improved statistical precision for all measurements and a anticipated integrated luminosity increase from Run 2 $\mathcal{L}^{Pb-Pb}_{integrated} = 1\,\mathrm{nb}^{-1}$ to Run 3 $\mathcal{L}^{Pb-Pb}_{integrated} = 6\,\mathrm{nb}^{-1}$ [18; 19].

2.1 Inner Tracking System 2

The ITS2 is the innermost detector currently installed in ALICE. It represents the second iteration of this detector, with the inner barrel expected to operate until the end of the current physics run (Run 3), while the outer barrel will continue in Run 4. A photograph of the ITS2 inner half-barrel is shown in Figure 2.2. The innermost layer has a diameter of 23 mm.

The key component of the ITS2 is the ALICE Pixel Detector (ALPIDE), a CMOS Monolithic Active Pixel Sensor (MAPS) and a fully digital sensor. Each ALPIDE pixel, sized 29.24 µm × 26.88 µm, includes a built-in amplifier, shaping stage, discriminator, and multi-event buffer [20].

To achieve coverage along the z-axis, multiple ALPIDE sensors are tiled end-to-end to form a stave. In the inner barrel, nine ALPIDE sensors, together with cooling, power, and support components, form a single stave. These staves are arranged in a half-cylindrical layer to construct the ITS2 inner barrel, with overlapping edges to enhance acceptance. Figure 2.3 shows the material budget distribution of a single layer of the ITS2 inner barrel across an azimuthal angular acceptance range of $0° < \phi < 60°$, with contributions from different components color-coded. This range corresponds to two staves. The distribution is highly irregular. Regions where staves overlap, as well as regions where the water cooling pipes are present are clearly visible as large contributors to the material budget. As shown, the average material budget for one layer of the ITS2 inner barrel is approximately $x/X_0 = 0.35\,\%$. [21].

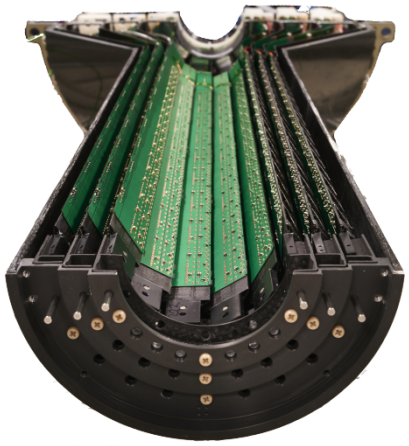

Figure 2.2: Photo of the Inner Barrel of the ITS2 [22].

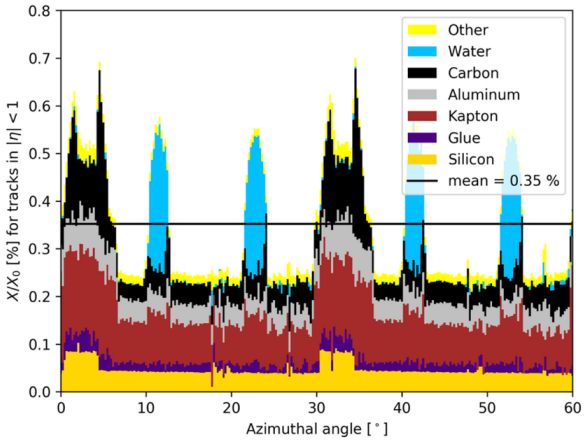

Figure 2.3: Material budget of one layer of the Inner Barrel of the ITS2 [4].

2.2 Motivating the step from ITS2 to ITS3

With the replacement in LS3 of the inner-most three layers of the ITS2 with the ITS3 the detector will be moved closer to the interaction point and has reduced material budget. With this the impact parameter resolution will be reduced by a factor of 2, bring a higher track reconstruction efficiency for low-momentum particles with it. This will improve the capability for heavy-flavor hadrons and dilepton measurements. As heavy-flavor hadron are mostly short lived they need to be measures via their decay products. Therefore improving the resolution on the primary and secondary vertices also improves the measurement of those particles. Heavy-flavor quarks, such as charm and beauty, are produced in the early stages of the collision and serve as sensitive probes for the properties of the QGP. Their interactions with the medium can provide crucial information about the transport properties of the plasma and the mechanisms of energy loss in the medium. Dileptons provide valuable information about the full time evolution of the medium as they do not interact strongly and are emitted through all stages of the collision.

The reduction in material budget offered by the ITS3 is essential for enhancing the detection of low-momentum particles. Low-momentum particles are key to understanding the collective behavior and hydrodynamic flow of the QGP, as they represent the majority of the matter produced in the collision. By improving the resolution and efficiency for these particles, the ITS3 enables more detailed studies of the thermalization process and the QGP's evolution over time. The improved vertex resolution and low material budget of the ITS3 are crucial for isolating these signals from the dense background of charged particles produced in heavy-ion

collisions [5].

2.3 Inner Tracking System 3

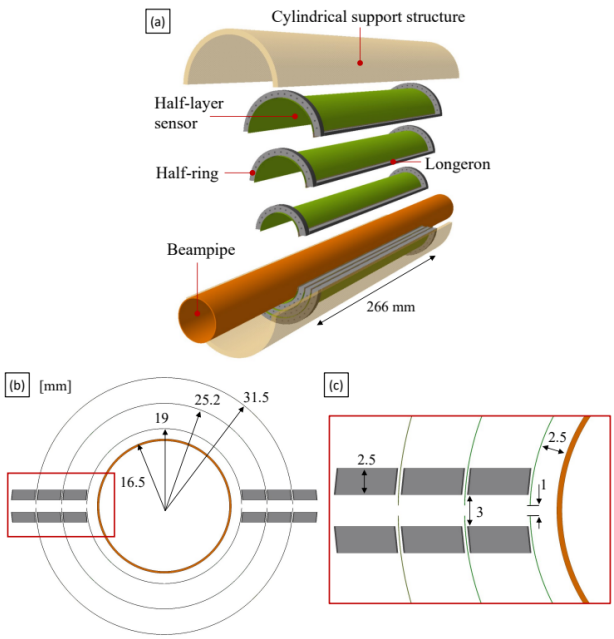

Figure 2.4: Simplified ITS3 detector layout, (a) half-layers around the beam pipe with carbon foam support structures, (b) radial view and (c) zoomed in view; from [5].

The ITS3 will be the first detector ever that will feature wafer-scale, bent silicon sensors of up to 26 cm × 10 cm, which are held in place by structural components consisting of carbon foam. The whole assembly is lightweight and will be cooled by forced airflow. Figure 2.4 shows a schematic layout of the ITS3 . The carbon foam will be placed on the sides of the detectors, not only to keep the different layers at their intended radii, but also forcing them into their cylindrical shape. Two carbon foam "longerons" which run length-wise in the z direction, parallel to the beam pipe, will be placed for each of the six sensors, as shown in the Figure 2.4. Their role is to ensure that the sensor remains evenly bent without introducing warping, an issue observed in earlier design models that used multiple pieces instead of a single longeron [5]. At the two end caps, the carbon foam "half-rings" are shaped as half-rings to define the radii. The half-rings will be placed on the A-side and C-side, which act as the end caps in forward and backward rapidity. The difference between A- and C-side come from the fact that the detectors in ALICE can only be accessed from one side, the A-side, due to the muon arm, which are a number of detectors dedicated to muon measurements

added on the C-side of ALICE, visible on the right side in Figure 2.1. This not only restricts the access, but also the powering, cooling and data lines, which need to be interfaced at the A-side.

As carbon foam is ultra lightweight and will only be placed on the sides, the average material budget of a full half-layer of the ITS3 is decreased to 0.09 %. This reduction of the material budget is crucial for minimizing multiple scattering and energy loss of particles as they traverse the detector. The upgrade not only replaces the innermost detector layers of the ITS2 with the ITS3 but also introduces a smaller beam pipe, positioning the innermost sensors closer to the interaction point. With this change, the cylindrical sensors are placed at distances of 19 mm, 25.2 mm, and 31.5 mm from the interaction point. This new cylindrical layout and reduced material budget directly improves the precision of both primary and secondary vertex reconstruction, which is fundamental for identifying and studying short-lived particles, e.g. heavy-flavor hadrons [4; 5; 23].

2.4 Material budget of the ITS3

For each half-layer, there are four regions with different material budget requirements: the region containing only the sensor, the longeron, and the A- and C-side half-rings. The A- and C-side half-ring carbon foams differ in their radiation lengths due to their varying densities, making them ideal for specific detector regions. As detailed in the Technical Design Report (TDR) [5], the carbon foam half-rings enhance heat exchange with the airflow by increasing the surface area in contact. K9 foam is chosen for the A-side's high-power dissipation area, prioritizing thermal conductivity ($\kappa_{f,K9} = 25\,\mathrm{W\,m^{-1}\,K^{-1}}$). RVC foam on the other hand has a lower thermal conductivity ($\kappa_{f,RVC} = 0.05\,\mathrm{W\,m^{-1}\,K^{-1}}$), but also a lower density and therefore a reduced material budget. This is needed because it is directly placed on the sensor's edge at the C-side half-rings and the longerons. This design balances the thermal and structural requirements across different regions of the detector.

Different projections of the simulated material budget encountered by particles traversing the innermost half-layer of the ITS3 are shown in Figure 2.5. Figure 2.5a shows a two-dimensional material budget distribution for particles originating from the interaction point at $z_{vtx} = 0$. The graph shows the material budget budget dependent on the azimuthal angle ϕ (y-axis) and pseudorapidity η (x-axis), with blue regions indicating a low material budget and red regions a higher material budget. As pseudorapidity η increases, the material budget also rises due to the longer path length within the material caused by the changing incident angle. In the silicon-only region, azimuthal symmetry ensures that the material budget does

not vary with ϕ. However, the contributions from the longeron structures are visible at the top and bottom of the distribution.

A projection within $|\eta| < 1$ of one half-layer for $0 < \phi < \pi$ is shown in Figure 2.5b. Here, the baseline material budget is determined by the silicon sensor, while the edges reveal contributions from the longerons, the carbon foam, and the glue securing the foam in place. These structures are the only components that increase the average material budget above the sensor's baseline. Figure 2.5c shows the material budget averaged over $0 < \phi < \pi$ as a function of pseudorapidity η. In this projection, the sensor dominates the material budget at higher η values. In Figure 2.5d, the material budget at $\eta = 0$ and $\phi = \pi/2$ is plotted, where the baseline contribution from the sensor is augmented by the half-ring structures at the sensor's edges. Across all cases, it becomes evident that the glue used in combination with the carbon foam structures significantly contribute to the material budget. However, these carbon foam holding structures only affect the edges of the sensor, with the sensor itself dominating the material budget in higher η regions.

While the anticipated thicknesses of all components intended for the ITS3 are documented in the TDR [5], the simulation shown in Figure 2.5 appears to exclude some components. According to the TDR, the carbon foam is first bonded to a carbon fleece using glue—a velcro-like material that serves as a barrier when applying a second glue layer. This step is essential as the fleece helps control the amount of glue seeping into the carbon foam's pores. The second layer of glue then connects the carbon fleece-foam assembly to the sensor. For the longeron, an additional polyimide film is used. It appears that at least the carbon fleece and the polyimide film are not included in the simulation.

Furthermore, the simulation estimates the radiation length and material budget of the components, but these properties require experimental verification. To validate them, a mockup sample is built, and a scattering experiment is conducted to measure the material budget and radiation lengths of the components used in constructing the ITS3 . This approach ensures that the simulated values are consistent with the actual properties of the materials.

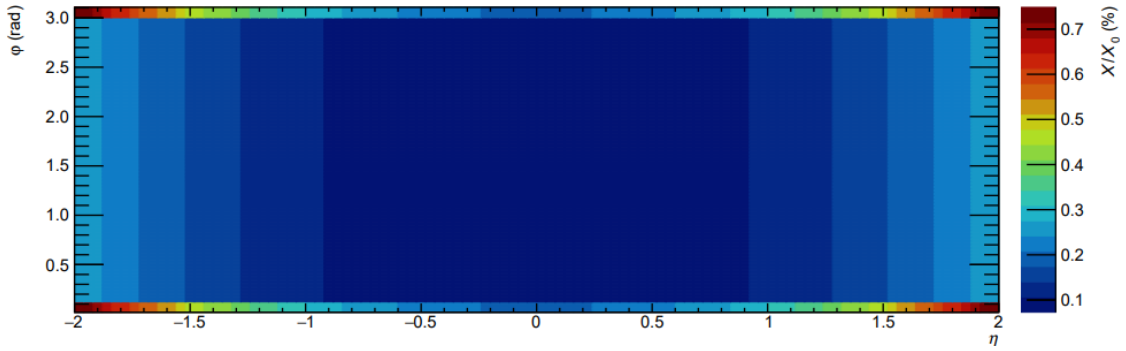

(a) Material budget for tracks of particles originating from the interaction point $z_{vtx} = 0$ as a function of ϕ (rad) and η.

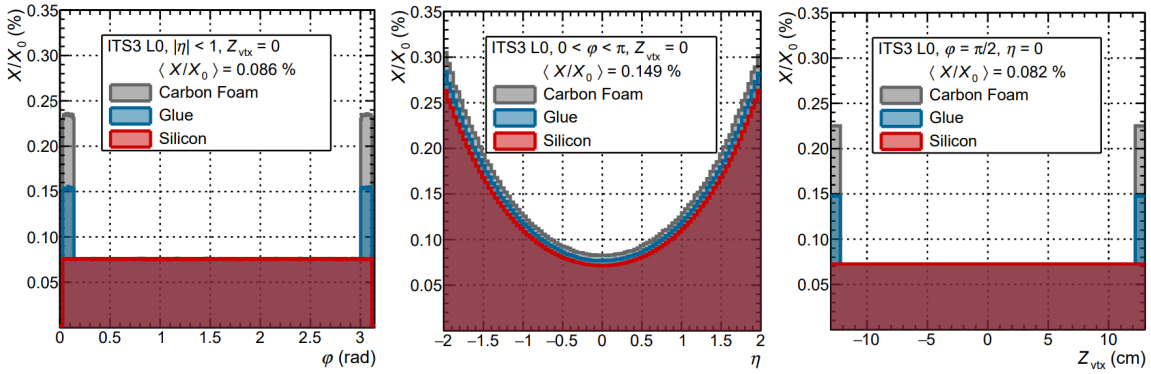

(b) Averaged material budget for $|\eta| < 1$ of particles originating from the interaction point $z_{vtx} = 0$ as a function of ϕ (rad). With an average $\langle x/X_0 \rangle$ of 0.086% for $z_{vtx} = 0$, $|\eta| < 1$ and $0 < \phi < \pi$.

(c) Averaged material budget for $0 < |\phi| < \pi$ of particles originating from the interaction point $z_{vtx} = 0$ as a function of η. With an average $\langle x/X_0 \rangle$ of 0.149% for $z_{vtx} = 0$, $|\eta| < 2$ and $0 < \phi < \pi$.

(d) Averaged material budget for $\eta = 0$ and $\phi = \pi/2$ as a function of $z_{vtx} = 0$. With an average $\langle x/X_0 \rangle$ of 0.082% for $|z_{vtx}| < 14\,\text{cm}$.

Figure 2.5: Simulation of the material budget for tracks with different origins evaluated for half-layer 0 from [5].

3 Test beam campaign: sample & setup

3.1 Sample preparation

To determine the radiation length of various components of the ITS3, a mockup sample was constructed instead of using a fully assembled ITS3. This decision was guided by several considerations. The high production cost of a complete ITS3 , and the limited measuring area of the telescope, restricted to the size of an ALPIDE chip (approximately $3 \times 1.5\,\text{cm}$), necessitated a smaller sample. Furthermore, the constrained time available at the test beam facility made it more efficient to combine different regions of the ITS3 into a single mockup sample.

The mockup was designed to include only the RVC carbon foam, as the K9 carbon foam is not located in the sensing region of the ITS3 and was studied before [10], therefore it was excluded. As a result, the "half-ring" region in the mockup represents only the C-side. Three distinct regions were selected for the sample: the **sensor-only** region, the **C-side "half-ring"** region, and the **"longeron"**. Both sensors used in the mockup were non-working dummy ER1 sensors, simplifying the construction while preserving the relevant material composition for the study.

The mockup samples were prepared in collaboration with ITS3 colleagues at CERN, using the same amount of materials that would later be used in building the ITS3. The process began by combining the carbon foam with carbon fleece (see Figure 3.1a). The carbon fleece was soaked in Araldite 2011 glue, which results in 70 µm of glue per fleece, with an additional 50 µm layer of glue applied. This resulted in a total glue thickness of 120 µm for each layer of carbon fleece. The extra glue seeped into the foam, ensuring a robust bond between the fleece and the foam. The glue-treated fleece was then applied to both sides of the carbon foam and left to cure. After curing, the fleece formed a hard layer on the foam, creating a barrier that prevented further glue penetration. This step ensured precise control over the amount of glue used in subsequent layers.

In all glue application steps the same method is used (see Figure 3.1b). A block with a height equal to the desired glue thickness plus the height of the object where the glue is being applied to was placed next to the object. Glue was applied, and any excess was removed in a single continuous motion using a razor blade.

After preparing the foam and fleece structure, it was combined with the dummy sensor. The sensor without any foam layers is shown in Figure 3.1c. For the longeron region, which includes an additional polyimide strip (yellow tape on the left side of the sensor in Figures

3.1), the amount of glue applied differed between the two sides of the sample. On the left side, corresponding to the longeron, 70 µm of glue was applied, while the right side, corresponding to the half-ring, required 140 µm of glue. Figure 3.1d shows the foams and the holding structure attached to the lower dummy sensor and the final assembly with foam layers and holding structures is displayed in Figure 3.1e. The polyimide tape is only applied on the lower sensor. In both cases, an additional 50 µm of glue was applied to attach the foam to the sensor. This additional glue helps to attach the foams to the sensor and is supposed to seep to the sides. The seeping glue can be seen in Figure 3.1e.
On top of that, an additional "big sample" was prepared to specifically measure the material budget of the foam. This sample was constructed using the same materials but including a foam layer that is 6 mm taller, enabling more detailed analysis of the foam's contribution to the overall material budget.

3.2 Estimation for components

Before the material budget of the whole sample can be calculated first the radiation lengths of the different materials need to be estimated as a cross-check to the TDR [5]. This is done by combining the known radiation lengths of the individual elements (Table 1) via Formula (5).

Table 1: Radiation lengths, masses and relative weights of essential elements (values from [13])

Element	Symbol	Radiation Length [g/cm^2]	Mass [g/mol]	Relative Weight [%]	
				Polyimide	Glue
Hydrogen	H	63.04	1.008	2.64	6.43
Carbon	C	42.7	12.011	69.11	76.57
Oxygen	O	34.24	15.999	20.92	17.00
Nitrogen	N	37.99	14.007	7.33	–
Aluminum	Al	24.01	26.982	–	–
Nickel	Ni	12.68	58.693	–	–
Silicon	Si	21.82	28.085	–	–

Sensor Even though the MAPS consists not only of silicon but also includes a few µm of aluminum metal lines on the top, it can be approximated as having an equivalent material thickness of 50 µm silicon. This assumption is reasonable because aluminum has a radiation

length similar to silicon. Also is the exact aluminum content proprietary information. Given the radiation length of silicon, $X_{0,Si} = 9.369\,\text{cm}$, and a sensor thickness of $(50 \pm 0.1)\mu\text{m}$, the material budget of a single sensor can be calculated. Since the uncertainty in the silicon radiation length is negligible compared to the uncertainty in thickness, it is disregarded. The material budget of one sensor is:

$$\left(\frac{x}{X_0}\right)_{sensor} = (0.534 \pm 0.001)‰. \tag{10}$$

In the samples there are two sensors used, therefore the material budget needs to be double that of one: $(x/X_0)_{2xsensor} = (1.067 \pm 0.002)‰$.

Polyimide For the polyimide, which has the chemical formula $C_{22}H_{10}N_2O_5$ the relative weights of each element is calculated with:

$$w_i = \frac{m_i \cdot n_i}{w_{tot}}, \qquad \text{with} \quad w_{tot} = \sum_j m_j \cdot n_j, \tag{11}$$

where m_i is the atomic mass of each element and n_i the atomic fraction of the element in the material. With the weights and the radiation lengths from Table 1 the radiation length is calculated to be $\widetilde{X}_{0,Polyimide} = 40.58\,\text{g/cm}^2$. With a density of $1.42\,\text{g/cm}^3$ [24] the radiation length is $X_{0,Polyimide} = 28.57\,\text{cm}$, which is consistent with other publications [25]. The thickness of the film is $x_{Polyimide} = (70 \pm 1)\mu\text{m}$, which results in a material budget of $(x/X_0)_{Polyimide} = (0.245 \pm 0.003)‰$.

Araldite 2011 The glue that binds all components together is Araldite 2011, which is a two component epoxy glue, and has a density of $\rho_{Glue} = 1.05\,\text{g/cm}^3$ [26]. Because the correct chemical formula of Araldite 2011 is proprietary, the radiation length has to be approximated by a good guess of the correct chemical formula. One good guess would be to assume a phenol formaldehyde resin which has the chemical formula C_6H_6O. The weights are calculated the same way as in Formula (11) and are shown in Table 1. The radiation lengths comes to be $\widetilde{X}_{0,Glue} = 41.81\,\text{g/cm}^2$ which is in this case $X_{0,Glue} = 39.82\,\text{cm}$. Because measurements conducted by other groups vary a bit [5], an error on the radiation length of $X_{0,Glue} = (40 \pm 1)\text{cm}$ is assumed.
The thicknesses of the different glue layers can be found in Table 2. Because the application process of the glue can not be precisely controlled, a thickness uncertainty on each applied layer of glue of $\sigma(x_{Glue}) = 30\,\mu\text{m}$ is assumed.

Carbon fleece The carbon fleece used here has an areal weight of $m_A = 8\,\mathrm{g/m^2}$ and according to measurements done at CERN a thickness of $x_{fleece} = (70 \pm 1)\mu\mathrm{m}$. Therefore its density is $\rho_{fleece} = m_A/x_{fleece} = 0.114\,\mathrm{g/cm^3}$ and the radiation length can be calculated with:

$$X_{0,fleece} = \frac{\widetilde{X}_{0,Carbon}}{\rho_{fleece}} = \frac{\widetilde{X}_{Carbon} \cdot x_{fleece}}{m_A} \quad \text{and} \quad \sigma(X_{0,fleece}) = \frac{\widetilde{X}_{Carbon}}{m_A} \cdot \sigma(x_{fleece}). \tag{12}$$

This leaves the radiation length to be $X_{0,fleece} = (374 \pm 5)\mathrm{cm}$. Here the air is not considered, as the air will be replaced by glue in the process of building the sample. The material budget of the carbon fleece comes to be $(x/X_0)_{fleece} = (0.0374 \pm 0.0004)‰$

Carbon foam To estimate the material budget of the foam the specifications of the manufacturer are needed. The foam used is the Duocell© Reticulated Vitreous Carbon (RVC) foam by ERG, which has a relative density of 3 % and a pore count of 100 PPI (pores per inch). From measurements done at CERN the density of the foam could be put in the range between $0.046\,\mathrm{g/cm^3} \leq \rho_{foam} \leq 0.0479\,\mathrm{g/cm^3}$. With that the radiation length of the foam can be estimated with Formula (12) to be $(910 \pm 20)\mathrm{cm}$. The anticipated thickness is $x = 5.68\,\mathrm{mm}$ and because it was sanded down by hand an uncertainty of $\sigma(x) = 50\,\mu\mathrm{m}$ is assumed. Therefore the material budget of the foam is $(x/X_0)_{\mathrm{foam}} = (0.62 \pm 0.02)‰$. For the big sample the same kind of carbon foam is used except that it is 6 mm thicker. For that the material budget can be estimated to be $(x/X_0)_{\mathrm{big\ foam}} = (1.28 \pm 0.03)‰$.

3.3 Material budget of the sample

The thicknesses, radiation lengths and material budgets of the sub components are summarized in Table 2. The material budget of the full carbon foam support structures in the sample are calculated using Formula (6) and its uncertainty according to Formula (7). The biggest uncertainty comes from the thickness of the glue, because the application process could only guarantee an accuracy of $\sim 30\,\mu\mathrm{m}$.

Half-ring The half-ring is symmetric on both sides and consists of carbon foam, carbon fleece and glue. Its material budget is estimated as:

$$\left(\frac{x}{X_0}\right)_{\text{Half-Ring}} = (2.0 \pm 0.2)‰ \quad \text{and with the sensors:} \left(\frac{x}{X_0}\right)_{\text{Half-Ring + Sensor}} = (3.0 \pm 0.2)‰$$

Table 2: Estimated contribution of the sample components to the material budget

Element	Component	Material	**Thickness** x [µm]	X_0 [**cm**]	x/X_0 [‰]
Sensors	MAPS	Silicon (equivalent)	$2 \times (50 \pm 1)$	9.369	1.067 ± 0.002
Half-ring	Carbon foam	Carbon (RVC) Duocell©	5680 ± 50	910 ± 20	0.62 ± 0.01
		2×Araldite 2011 (penetration)	$2 \times (50 \pm 30)$	40 ± 2	0.3 ± 0.1
	Interface layer	2×Carbon fleece	$2 \times (70 \pm 1)$	374 ± 5	0.0374 ± 0.0005
		2×Araldite 2011 (penetration)	$2 \times (70 \pm 30)$	40 ± 2	0.4 ± 0.1
	Gluing layer	2×Araldite 2011	$2 \times (140 \pm 30)$	40 ± 2	0.7 ± 0.1
			6100 ± 70	310 ± 3	2.0 ± 0.2
		with Silicon	6200 ± 70	204 ± 2	3.0 ± 0.2
Longeron	Carbon foam	Carbon (RVC) Duocell©	5680 ± 50	910 ± 20	0.62 ± 0.01
		2×Araldite 2011 (penetration)	$2 \times (50 \pm 30)$	40 ± 2	0.3 ± 0.1
	Interface layer	2×Carbon fleece	$2 \times (70 \pm 1)$	374 ± 5	0.0374 ± 0.0005
		2×Araldite 2011 (penetration)	$2 \times (70 \pm 30)$	40 ± 2	0.4 ± 0.1
	Gluing layer	Araldite 2011 (Top)	140 ± 30	40 ± 2	0.4 ± 0.1
		Araldite 2011 (Bottom)	70 ± 30	40 ± 2	0.2 ± 0.1
	Holding strip	Polyimide	70 ± 1	29 ± 2	0.245 ± 0.004
			6100 ± 70	300 ± 3	2.0 ± 0.2
		with Silicon	6200 ± 70	200 ± 2	3.1 ± 0.2

Longeron The longeron, in contrast, is asymmetrical, with less glue and an additional layer of polyimide tape. Since polyimide tape has a shorter radiation length than the glue it replaces, the total radiation length of the longeron is slightly reduced compared to the half-ring. This results in a slightly increased material budget for the longeron:

$$\left(\frac{x}{X_0}\right)_{\text{Longeron}} = (2.0 \pm 0.2)‰ \quad \text{and with the sensors:} \quad \left(\frac{x}{X_0}\right)_{\text{Longeron + Sensor}} = (3.1 \pm 0.2)‰$$

Big sample The components and construction of the big sample follow the one of the small sample, with the exception that the carbon foam is 6 mm thicker. This modification was specifically intended to estimate the radiation length of the carbon foam alone, by comparing the small and big samples at the same configuration parameters. The resulting material budget for the big half-ring and the big longeron, including the sensors, is determined to be:

$$\left(\frac{x}{X_0}\right)_{\text{big Half-Ring}} = (3.7 \pm 0.2)‰ \quad \text{and} \quad \left(\frac{x}{X_0}\right)_{\text{big Longeron}} = (3.8 \pm 0.2)‰ \tag{13}$$

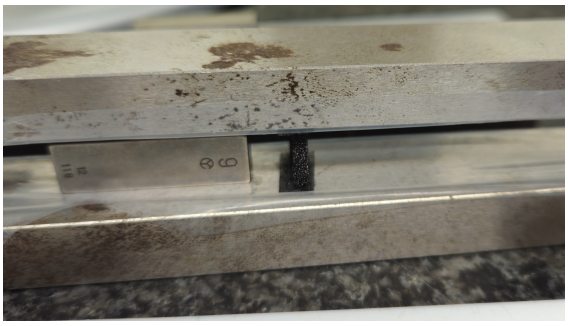

(a) Curing of the carbon foam with fleeces added with glue on both sides.

(b) Adding glue on the cured foam + fleece.

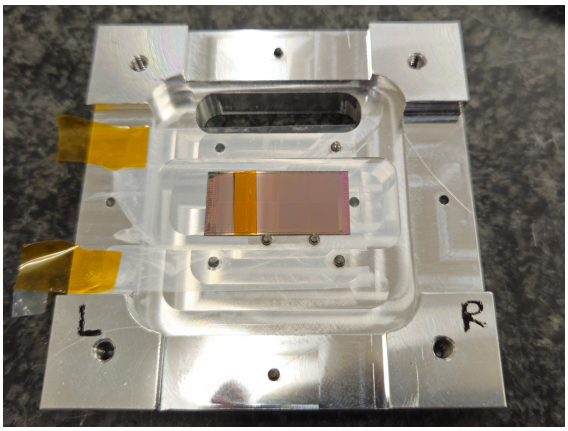

(c) Sensor with kapton tape glued on.

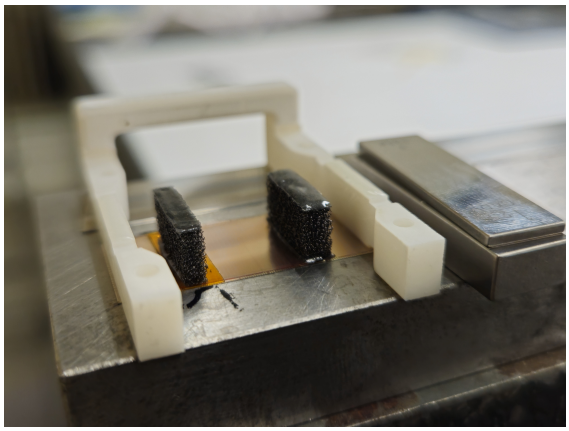

(d) Carbon foam with glue attached to the sensor. The holding structure is also visible.

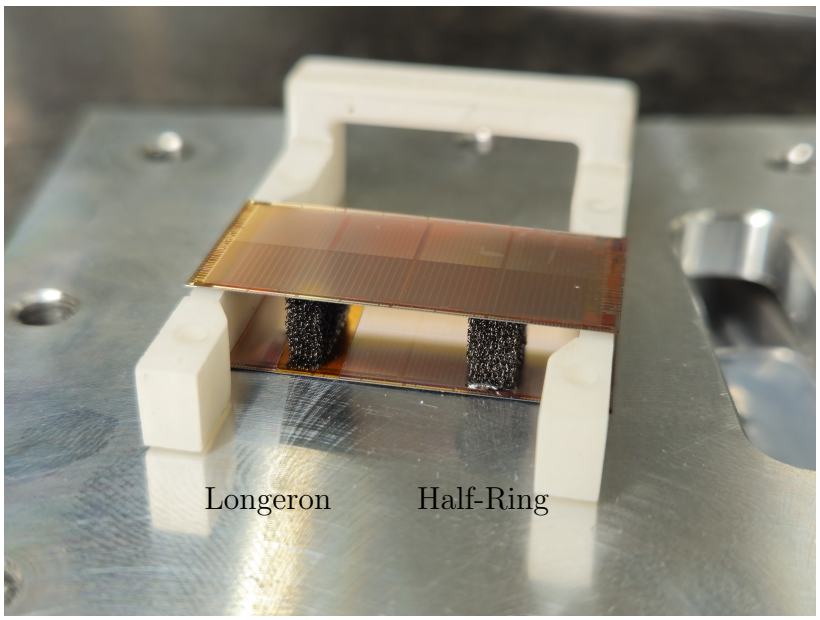

(e) Final sample

Figure 3.1: Step-by-step sample building process

3.4 Telescope optimization

The quantity that needs to be measured in this analysis is the angle between the incoming track and the outgoing track. Therefore, the measurement is highly dependent on the angular resolution and not only on the pointing resolution of the telescope. For this reason, the setup was optimized to achieve the best possible angular resolution with the available tools. Six ALPIDE sensors were used, and to maximize the resolution, all six were integrated into a symmetrical telescope setup. The mechanical constraints defined a minimal distance of 15 mm between the sensing plane and the target and 20 mm between two sensing planes. To determine the optimal configuration for the best angular resolution, a three-dimensional grid search was conducted using the software package from [27]. The software provides the convoluted resolution - the combined effect of both the intrinsic resolution and the scattering of present materials (the sensors silicon and air). It was observed that the key factor in achieving good angular resolution is having on both sides one measurement point as close as possible to the target and two additional measurement points positioned as close as possible together and further away, serving as a lever arm. Figure 3.2 shows a sketch of the telescope geometry with distances used during the test beam. Sensors A3 and A4, closest to the target, have their distances to the target (A3-target and target-A4) mechanically restricted to a minimum of 15 mm. The distances between the outer sensors (A1-A2 and A5-A4) are mechanically limited to at least 20 mm. By fixing the distances between the outer ALPIDE sensors (A1-A2 and A4-A5) and between the target and the closest sensors (A3-target and target-A4), the angular resolution was evaluated by varying the lever arm distances (A2-A3 and A3-A4). The varying resolution is illustrated in Figure 3.3. Initially, the resolution improves as the lever arm helps to resolve the trajectory. However, as the distance increases further, the resolution worsens because the benefit of the lever arm diminishes. The optimal distance for the telescope is chosen where the resolution reaches its minimum. For a higher energy, as seen when comparing Figure 3.3a and Figure 3.3b, the optimal distance of the lever arm increases. This is due to the narrower scattering angle distribution at higher momentum (see Highland (8): $\theta_0 \sim 1/p$) resulting in smaller overall scattering angles that can be better resolved with a longer lever arm. The symmetry of

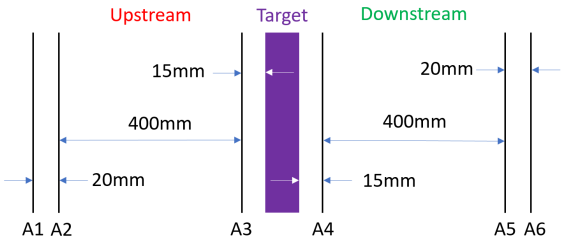

Figure 3.2: Illustration of the geometry of the telescope used in this thesis.

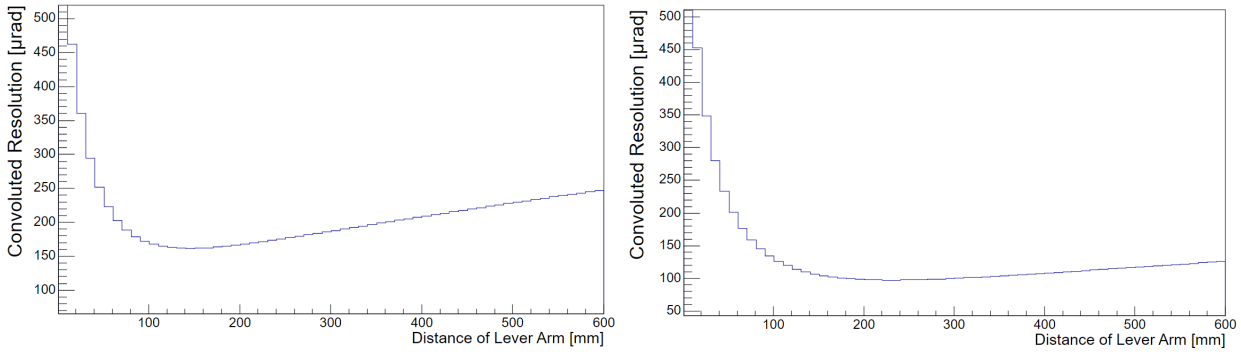

(a) Energy = 2.4 GeV **(b)** Energy = 4.8 GeV

Figure 3.3: Convoluted angular resolution for two energies and different distances between plane A2 to A3 and plane A4 to A5 ("lever arm"), while the other distances are fixed at 20 mm for A1 to A2 and A5 to A6 and 15 mm for A3 to target and target to A4. Performed with the telescope simulator [27].

the telescope setup was also determined through the grid search optimization. It was found that the resolution does not significantly change due to the energy loss in the target; thus, any small differences in resolution for different energies were neglected. It was chosen to use one symmetrical setup for both energies ($E = 2.4\,\text{GeV}$ and $E = 4.8\,\text{GeV}$), minimizing the need to adjust the telescope at the test beam site. Each access to the telescope could lead to minor misalignments of the sensors, as well as a loss of valuable beam time. The mean of the optimal values for both energies, determined during the grid search, are summarized in Table 3. These values are provided for a telescope situated in air and for one in helium. The geometric resolution obtained from the simulation includes the convolution with the scattering contribution in the respective medium (air or helium). As the radiation length increases (e.g., in helium), the lever arm distance for optimal resolution tends to increase. This is because reduced scattering in a medium with higher radiation length results in smaller observed scattering angles. With less angular broadening, a longer lever arm becomes advantageous, improving the angular resolution.

A crucial mistake that was only realized after the test beam campaign was that a flag for the main scatterer was incorrectly set during the setup optimization. The configuration chosen for the test beam assumed the main scatterer to be helium. However, at the DESY test beam area, the environment is filled with air, not helium. This mistake had a significant impact because the optimal configuration for angular resolution differs between air and helium due to the differences in scattering properties. By mistakenly assuming helium, the chosen setup had sensor distances optimized for minimal scattering effects, which is not the case

Table 3: Distances of the telescope planes for highest angular resolution in helium and air

		Distance between planes	
Upstream	Downstream	Helium	Air
A1 - A2	A5 - A6	20 mm	20 mm
A2 - A3	A4 - A5	400 mm	165 mm
A3 - Target	Target - A4	15 mm	15 mm

in an air-filled environment. Consequently, the actual resolution of the test beam setup is worse than initially anticipated. As a result, for an energy of $E = 2.4\,\text{GeV}$, the convoluted angular resolution is about $\sigma_{\text{angular}} \approx 210\,\mu\text{rad}$, and for $E = 4.8\,\text{GeV}$, it is approximately $\sigma_{\text{angular}} \approx 105\,\mu\text{rad}$. These values reflect the misalignment of the chosen setup with the actual air environment, leading to a suboptimal resolution compared to what could have been achieved with an air-optimized configuration.

3.5 Measurement statistics

To maximize the use of the one-week test beam period available in April 2024 at DESY, a quick calculation of the required statistics was performed to estimate the time needed for each target to be inserted. According to previous studies on the characteristics of the test beam areas [28], the highest particle rate is observed at 2 GeV. Since earlier studies were conducted at 2.4 GeV on previous versions of the ITS3 sample [10], this energy was selected to allow for direct comparison and serve as a reference, despite the minor reduction in particle flux, which comes to be about $f_{\text{flux,2.4GeV}} \approx 3.8\,\text{kHz}\,\text{cm}^{-2}$ [28]. To enable a direct comparison with data collected using the same telescope geometry during the same test beam campaign, a measurement at a higher energy of 4.8 GeV was also selected, which yields a particle flux of about $f_{\text{flux,4.8GeV}} \approx 1\,\text{kHz}\,\text{cm}^{-2}$[28]. The choice to double the energy was arbitrary, intended to facilitate a simpler comparison between the two datasets, as the observed angles should theoretically scale by a factor of 2 (see Equation (8)). The primary criterion was ensuring a sufficient gap between the two energies, so the measurements would have a clear distinction. One goal of this thesis is to do the material budget analysis differentially on a cell by cell basis, to observe material budget fluctuations. To estimate the material budget a gauss fit is performed to estimate the scattering angle distribution. For that adequate statistics are needed to create a robust estimator. Therefore a minimum amount of tracks intersecting at each cell is required to get a good estimate of the scattering angle distribution. For a

wanted number of entries per cell $n_{\text{entries per cell}}$ the number of total particles that need to be observed can be easily calculated to be $n_{\text{observe}} = n_{\text{cells}} \cdot n_{\text{entries per cell}}$. Because only a part of the particles that come out of the beam line produces a track that can be used later in the analysis, this efficiency fraction needs to be accounted for f_{eff}. Therefore the total number of incident particles n_{total} can be estimated to be:

$$n_{\text{total}} = n_{\text{cells}} \cdot n_{\text{entries per cell}} \cdot \frac{1}{f_{\text{eff}}} \tag{14}$$

$$= \frac{A_{\text{sensing}}}{A_{\text{cell}}} \cdot n_{\text{entries per cell}} \cdot \frac{1}{f_{\text{eff}}}, \tag{15}$$

with A_{sensing} and A_{cell} being the areas of the sensing area and a single cell respectively. To convert the particle flux into a particle rate, the estimated flux is multiplied by the area of the sensor:

$$r_{\text{rate}} = f_{\text{flux}} \cdot A_{\text{sensing}} \tag{16}$$

Therefore the time $t_{\text{target,E}}$ that is needed for all cells of one target at a specific energy to have a certain number of entries can be calculated with:

$$t_{\text{target,E}} = \frac{n_{\text{total}}}{r_{\text{rate}}} \tag{17}$$

$$= \frac{n_{\text{entries per cell}}}{A_{\text{cell}} \cdot f_{\text{flux}} \cdot f_{\text{eff}}} \tag{18}$$

Because the only thing that varies for one target will be the flux due to the change in energy, the total time t_{target} that is needed for each target can be calculated to be:

$$t_{\text{target}} = \frac{n_{\text{entries per cell}}}{A_{\text{cell}} \cdot f_{\text{eff}}} \cdot \left(\frac{1}{f_{\text{flux,2.4GeV}}} + \frac{1}{f_{\text{flux,4.8GeV}}} \right) \tag{19}$$

To get the total time needed the individual times for each target are added together:

$$t_{\text{total}} = \sum_{\text{targets}} t_{\text{target}} \tag{20}$$

This formula can be simplified when all targets have the same cell size. The number of entries that one would get for a given size of each cell and a given total test beam time can then be calculated by inverting the formula of the total time:

$$n_{\text{entries per cell}} = \frac{1}{n_{\text{targets}}} \cdot \frac{t_{\text{total}} \cdot A_{\text{cell}} \cdot f_{\text{eff}}}{\left(\frac{1}{f_{\text{flux,2.4GeV}}} + \frac{1}{f_{\text{flux,4.8GeV}}} \right)} \tag{21}$$

The test beam campaign was scheduled to last one week. After accounting for the time required for the assembly and disassembly of the telescope, target changes, accelerator maintenance, and a buffer for unforeseen delays, approximately six full days of data collection

remained. For the ITS3 samples, the goal was to achieve a cell size of $A = 100\,\mu\text{m} \times 100\,\mu\text{m}$ to resolve glue structures in the carbon foam. With an estimated efficiency of $f_{\text{eff}} = 70\,\%$ (due to the acceptance of the detector and tracking efficiency) and the measurements planned for five configurations (two ITS3 samples, two calibration targets, and one "empty" telescope arrangement with only air), this configuration would yield approximately $6,000$ entries per cell. While this number would be sufficient to perform a robust Gaussian fit of the scattering curve, variations in particle flux across the sensing area were expected. To account for these variations, it was decided to target an average of at least $10,000$ entries per cell for reliable results. To achieve this, the cell size for the calibration targets and the empty telescope configuration was adjusted to $A = 250\,\mu\text{m} \times 250\,\mu\text{m}$. Recalculating with this cell size using (20) yielded approximately $11,500$ entries per cell across all targets. This adjustment ensured that the planned measurements for both ITS3 samples, the two calibration targets, and the empty telescope setup could be accommodated within the time frame of the test beam campaign.

3.6 Test beam campaign

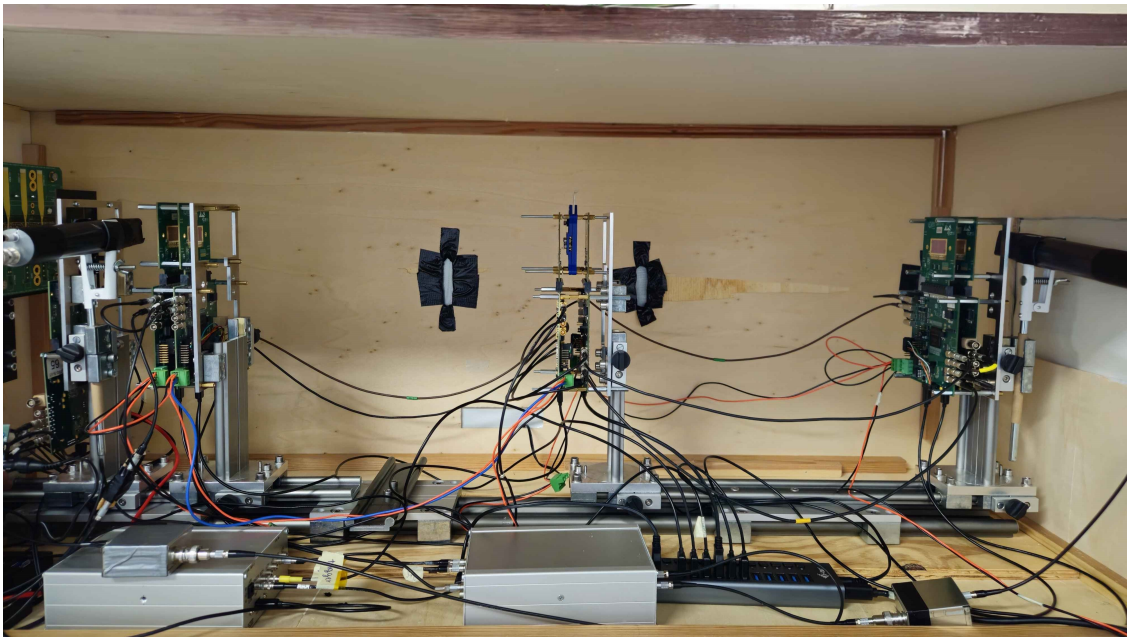

Figure 3.4: Telescope setup used at DESY. The e^- beam would be coming from the right.

The test beam data for this thesis was gathered at the Deutsches Elektronen-Synchrotron (DESY) facility, specifically in test beam area 24 during april 2024. Data collection spanned

an entire week but encountered periodic interruptions due to target exchanges and necessary accelerator maintenance. Additionally, unforeseen challenges, such as issues with the triggering at the start of the week, led to a reduction of the time allocated for data collection using the "empty" telescope configuration. The experimental setup used in this test beam can be seen in the Figure 3.4. The electron beam would come in from the right and after passing through a scintillator and the three upstream ALPIDE sensors on the right reach the target. The target with the blue holding structure can be seen in the middle. After scattering in the target the electrons would continue through the telescope first traversing the three downstream ALPIDE sensors and then the scintillator in the back. Only when both scintillators registered a hit in a certain time window the event would be triggered and stored. The selection ensures that only events containing particles which traversed all six ALPIDE sensors are stored, thereby reducing the overall data volume. On the left side an additional setup is present, decoupled from the measurements performed in this work. For the alignment of the telescope the test beam facility provides a laser guiding system and additional alignment is then done after setting everything up and looking at the beam profile observed with the telescope. The energy of the beam and the collimator setting is controlled by the user.

4 Calibration for material budget imaging

A calibration of the measurement is required, because the Highland formula, used to describe the multiple scattering inside the target, is accurate within uncertainties up to 11 % only within the range of $10^{-3} < x/X_0 < 100$ [16]. The ITS3 samples material budget, however, is near the edge of this validity range. By using the calibration targets, it is hoped that the effective validity range can be extended, enabling a measurement of the samples. To calibrate the measurements, two target materials with well-known thicknesses and radiation lengths were included in the scattering studies. Similar calibration targets have been successfully utilized in previous Material Budget Imaging (MBI) studies [11; 10], demonstrating their effectiveness in calibrating the measurement. For this thesis, calibration targets were selected with x/X_0 values both above and below those expected of the sample, enabling interpolation of the sample's x/X_0 value.

The chosen targets, made of 99.9% pure aluminum and nickel, are described in Table 4. Each target consists of layered sheets of the same material (aluminum or nickel), forming four horizontal regions with varying material budgets. For aluminum the sheet thicknesses are: 70 µm, 200 µm and 200 µm and for nickel: 25 µm, 50 µm and 90 µm. Horizontal regions were chosen because at the DESY test beam areas a horizontal momentum gradient is expected. Within each region, the material budget is expected to remain constant horizontally, ensuring that only the beam momentum changes across the region. This arrangement enables the study of momentum-dependent scattering effects. The targets are mounted in a blue holder (Figure 4.1) and positioned in the telescope at the same location as the sample to maintain consistent measurement conditions.

Figure 4.1 highlights the target structure: dotted yellow lines indicate region boundaries (described in Table 4), while the gray area represents the ALPIDE sensor's active region. The targets include four regions: an air-filled "empty" region and three with increasing material thicknesses.

Table 4: Thicknesses of the calibration target regions

	Aluminum			Nickel		
Radiation length X_0 [mm]	88.97			14.24		
Thickness x [mm]	0.07	0.27	0.47	0.025	0.075	0.165
Material Budget x/X_0 [‰]	0.79	3.03	5.28	1.76	5.27	11.59
Region	R1	R2	R3	R1	R2	R3

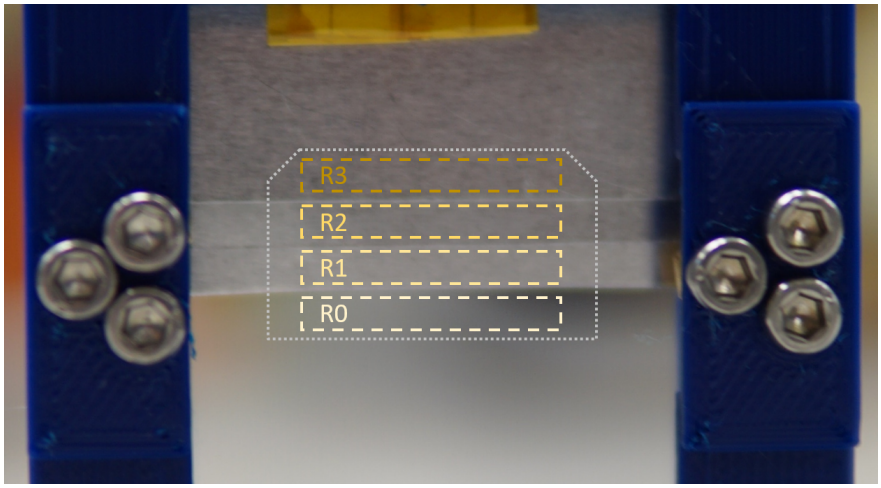

Figure 4.1: Picture of the calibration target holder with the aluminum targets; the measurable regions of different thickness (shades of yellow) and the ALPIDE sensing region (gray) are indicated.

4.1 Telescope alignment

A precise alignment of the telescope is critical for ensuring accurate tracking and reliable measurement results. While significant effort is made during the test beam campaign to match the positions of the ALPIDE planes and the target to the desired configuration, manual alignment can typically only achieve a positional accuracy of $\mathcal{O}(1\,\mathrm{mm})$. This level of precision is insufficient for high-resolution tracking, which requires knowledge of the telescope geometry at the scale of $\mathcal{O}(1\,\mu\mathrm{m})$. Consequently, an in-data tracking based alignment procedure is performed post-measurement using the *AlignmentTrackChi2* tool from the `Corryvreckan` software package [29].

The alignment process iteratively optimizes the positions and orientations of the telescope planes by minimizing the χ^2 of fitted tracks. The χ^2 is a measure of how well the observed data points match the expected positions along the fitted trajectory, and is defined as:

$$\chi^2 = \sum_{\text{planes}} \frac{(O_i - E_i)^2}{E_i} \tag{22}$$

where O_i is the observed position of the particle on the plane and E_i is the expected position based on the fitted track. The goal of the alignment is to reduce χ^2 to a minimum, indicating that the telescope geometry closely reflects the real positions and orientations of the ALPIDE planes.

The alignment procedure uses a General Broken Lines (GBL) tracking model, which is specif-

ically designed for experiments where multiple scattering plays a significant role. Unlike a simple straight-line fit, the GBL model incorporates deviations in particle trajectories caused by scattering materials, such as the silicon of the sensing ALPIDE sensors, the surrounding air and the target inserted in this experiment. By considering these deviations, the GBL model provides a more accurate representation of the particle's path, making it particularly advantageous for aligning the telescope geometry when the target is present. The GBL is a sophisticated track-fitting model that describes a particle's trajectory as a series of short, straight-line segments connected by "break points." These break points represent the locations where the particle undergoes significant scattering, such as in the sensor planes or the target. At each break point, the model accounts for the deflection of the particle, while also considering the uncertainties introduced by the measurement devices and material interactions.

During the alignment, tracks are fitted through all telescope planes, and the positions of the planes are iteratively adjusted in the x- and y-coordinates, while rotations are optimized in all three axes (x, y, z). The z-positions of the planes remain fixed during the alignment process due to the weak mode nature of the z-position in this telescope setup. A weak mode refers to a parameter that has minimal influence on the tracking resolution, making its optimization less effective in this context. Minor deviations in the z positions of the telescope planes have negligible effects on the alignment precision and tracking performance. One important consideration is that the alignment must be performed separately for each target. During target exchanges, the innermost ALPIDE planes near the target are moved, introducing possible small shifts in their positions and rotations. As a result, a new alignment is necessary for each target to ensure that the telescope geometry accurately reflects the setup during the corresponding measurement. By recalibrating the geometry for each target, the alignment procedure ensures consistency and precision across all datasets. To establish a stable global coordinate system for the telescope, the second plane is designated as the reference plane. This choice is motivated by the fact that, unlike the two planes closest to the target, the second plane remains untouched during target exchanges. By fixing this plane as the reference, the global coordinate system remains

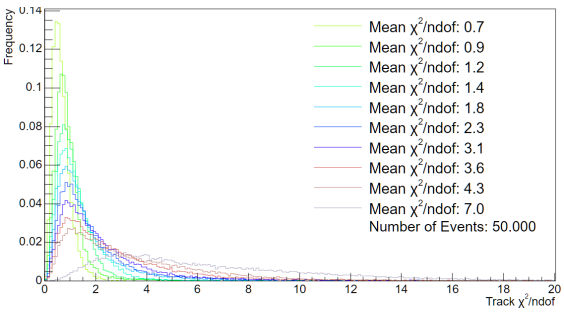

Figure 4.2: χ^2/ndof distributions for different alignment steps

consistent across different targets, facilitating straightforward comparisons of alignment results and subsequent analyses.
Figure 4.2 shows the χ^2/ndof distribution at different iteration stages of the alignment procedure. With each iterative step, the χ^2/ndof decreases, indicating that the alignment is progressively improving. This reflects the increasing accuracy of the telescope geometry model in mimicking the actual experimental setup. After a sufficient amount of alignment iterations when the χ^2/ndof does not change significantly anymore, this geometry is then used as the final geometry for tracking.

4.2 Measurement technique

With the aligned telescope the particle trajectories can be measured. This is done by fitting a straight line through the measurement points before the target (upstream) and after the target (downstream) separately. To define a track the upstream and downstream tracks need to lie within a certain distance at the position of the scatterer. In x and y direction the tracks need to have a distance of closest approach within $100\,\mu\text{m} \times 100\,\mu\text{m}$ and this point needs to lie in z in the region of the target. The target region in z is defined as the midpoint of the target. Another requirement is that all six sensors must have registered a hit in order to form a track. If all of those requirements are satisfied the track of the particle is defined and the three dimensional angle between upstream and downstream is measured.
It was chosen to use a straight line model instead of GBL as the additional flexibility that GBL introduces is compromised by the separation into upstream and downstream tracklets. This reduces the available planes for track finding to $n_{\text{planes}} = 3$. With only three planes, this might lead to overfitting, where the algorithm tries to model noise or small deviations as physical effects. This could result in unnecessary complexity without a significant gain in tracking accuracy and might even lead to angular resolution loss.
A sketch of the construction of such a track can be seen in Figure 4.3. The particle (gray dotted line) will pass through the different materials in the telescope and gets scattered. In the ideal case it will leave hits is all six sensing planes. By reconstructing the tracks upstream and downstream of the target the scattering angle θ can be measured. The scattering angle θ that will be measured is a three dimensional angle and can be projected onto θ_X and θ_Y, with x and y being the local orthogonal coordinates of the telescope such that $\theta_{\text{space}} = \sqrt{\theta_x^2 + \theta_y^2}$. x and y are defined to be in the plane of the sensors and Z in beam direction.
An example of a scattering distribution is shown in Figure 4.4b. The distribution includes only tracks that fall within a defined x-y region at the scatterer. To determine the width

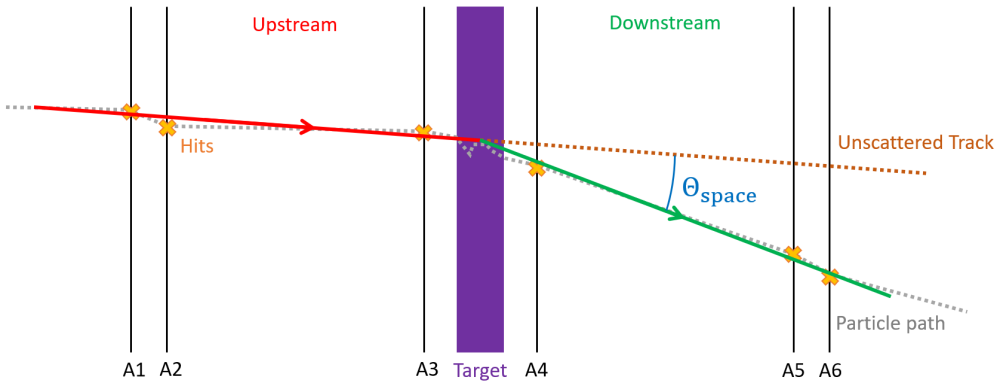

Figure 4.3: Projected sketch of track construction for upstream (red) and downstream (green) separately with angle measurement between them.

of this scattering distribution, a Gaussian fit is applied to the central 98 % of the data, and the standard deviation σ is extracted as an estimator of the width. While other estimators for the width have been explored in previous studies [10], the Gaussian fit proves to be one of the most reliable, especially when dealing with varying fit intervals. Furthermore, the factorization of the Highland formula by Lynch and Dahl [16; 13] was also done with that estimator and hence a Gaussian in the inner 98 % will be used for extracting the width of the distributions.

To capture fine details, small cells in the two dimensional plane with dimensions 100 µm × 100 µm (or 250 µm × 250 µm for targets with lower statistics: aluminum, nickel and "empty") are defined. Within each cell, the scattering angle distributions are created, and their widths, along with the associated fit uncertainties, are determined. These values are then stored based on the position of that cell. This process results in a two-dimensional map of the scattering angle distribution width for each target, with separate maps for the X and Y angles, as illustrated in Figure 4.4a.

In Figure 4.4a the different regions of aluminum are directly visible by eye, as the regions with more aluminum will result in a larger scattering angle. The regions are defined by the presence of uniform material. The first region at the top is an empty region where only scattering from air contributes. Further down is the next region with 70 µm of aluminum, followed by 270 µm and 470 µm equivalent. The different regions are visible and can be compared directly to the photo of the target in Figure 4.1. The scattering width map is compared to the photo vertically flipped, because the ALPIDEs are positioned upside down in the telescope due to their connection to the readout boards. Another feature are the two edges of PCB of the carrier cards of the sensors in the left and right bottom corner.

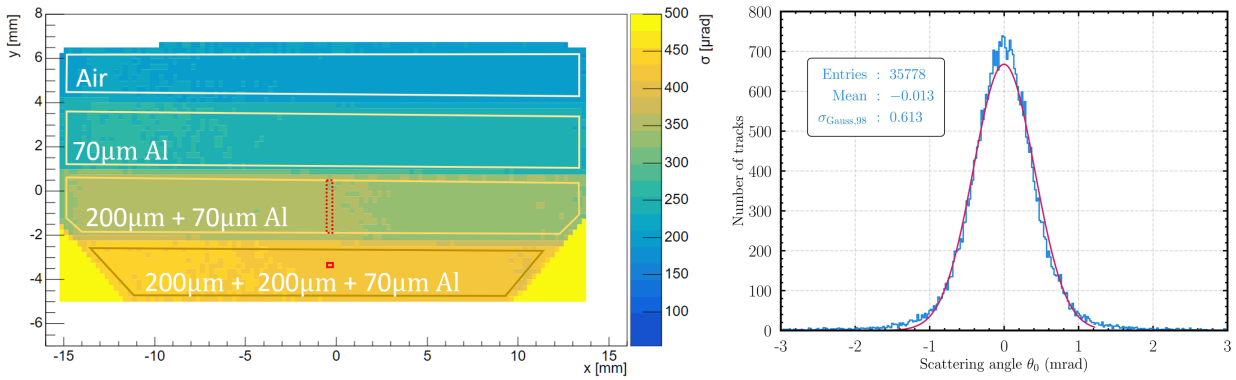

(a) 2D scattering distribution widths for X-angles of aluminum at $E = 2.4\,\mathrm{GeV}$

(b) Example Scattering Angle Distribution

Figure 4.4: Scattering distribution and resulting two dimensional maps for aluminum at $E = 2.4\,\mathrm{GeV}$

Those are two regions where the chip is glued to the carrier card, resulting in more material being present in the particles path and therefore scatting more. In Figure 4.4a and all other scattering angle width distributions only cells with distributions of more then 500 entries are considered, as the width estimate of a lower number of entries is more exposed to small fluctuations.

4.3 Quadratic subtraction

The measured angle distribution does not just contain the contribution of the target θ_{target}, but is a convolution of different kinds of effects. These include scattering in the surrounding air, contributions from the sensors, and other effects that can distort the distribution, all of which establish a background $\theta_{\text{background}}$ in the observed angle distribution. Additionally, systematic effects $\theta_{\text{systematics}}$, some of which remain partially unquantified, play a role. Finally, the telescope resolution $\theta_{\text{resolution}}$ introduces further smearing, broadening the overall distribution. The measured width of the angular distribution can be written as:

$$\theta_{\text{measured}} = \underbrace{\theta_{\text{Highland}}\left(\frac{x}{X_0}\right)}_{\theta_{\text{target}}} \circledast \underbrace{\theta_{\text{resolution}} \circledast \theta_{\text{background}} \circledast \theta_{\text{systematics}}}_{\theta_{\text{baseline}}} . \tag{23}$$

To get only the contribution of the target, a quadratic subtraction of the scattering angle widths between a baseline measurement θ_{baseline} where the target is not present and a measurement with the target θ_{measured} is performed:

$$\theta_{\text{target}} = \sqrt{\theta^2_{\text{measured}} - \theta^2_{\text{baseline}}}. \tag{24}$$

This procedure was already used in previous studies [11; 10] and turned out to be a step in the right direction. Of course, unfolding of the whole convolution of contributors would effectively leave only the target contribution, but until now there is no known formalism that can unfold this and reveal the material budget of the target. Therefore the scattering angles of a target in this thesis will be calculated by performing a quadratic subtraction. The uncertainty of both the measurement $\sigma(\theta_{\text{measured}})$ and the baseline $\sigma(\theta_{\text{baseline}})$ can be propagated with Gaussian error propagation:

$$\sigma(\theta_{\text{target}}) = \sqrt{\left(\frac{\theta_{\text{measured}}}{\theta_{\text{target}}} \cdot \sigma(\theta_{\text{measured}})\right)^2 + \left(\frac{\theta_{\text{baseline}}}{\theta_{\text{target}}} \cdot \sigma(\theta_{\text{baseline}})\right)^2}. \tag{25}$$

The quadratic subtraction for the target is performed on a cell-by-cell basis to account for and analyze fluctuations, such as momentum gradients, material budget variations, and statistical differences between cells. These material budget variations are particularly relevant for the ITS3 sample, where fluctuations are expected due to glue penetration into the porous carbon foam. Consequently, the analysis of the target region will consistently be conducted at the cell-by-cell level to capture these effects accurately. For example, to get the contribution of the scattering generated by 200 µm of aluminum the width of the distribution of 270 µm aluminum is quadratically subtracted from the distribution width of 470 µm aluminum. The value of the minuend (470 µm aluminum) is taken as the value of the cell with its uncertainty (red square in Figure 4.4a). To get the value of the subtrahend (270 µm aluminum) all cells within the same region at the same position in x (dotted rectangle in Figure 4.4a) are combined and the weighted mean and uncertainty of that slice is taken:

$$\mu = \frac{\sum \frac{x_i}{\sigma(x_i)^2}}{\sum \frac{1}{\sigma(x_i)^2}} \quad \text{and} \quad \sigma(\mu) = \frac{1}{\sqrt{\sum \frac{1}{\sigma(x_i)^2}}}, \tag{26}$$

with x_i being the values per cell with its uncertainty $\sigma(x_i)$. This value is then subtracted from the value of the cell of the minuend (470 µm Al) and the procedure is repeated for each cell of the desired region.

The combination of values for the baseline measurement is performed to eliminate local statistical fluctuations, ensuring consistent conditions. The same x-position of target and baseline is used due to the expected momentum gradient along the x-direction (addressed and corrected for in Chapter 5), as momentum is assumed to remain constant for a fixed x-position. If the two values were taken at different x positions, corresponding to different momenta, the subtraction could overestimate or underestimate the result due to the dependence $\theta_0 \sim 1/p$. This mismatch would introduce inaccuracies in the subtraction.

Additionally, resolution changes due to momentum must be considered. Since the measured value is convoluted with the resolution, subtracting measurements corresponding to different momenta would effectively subtract different resolutions, introducing errors. By using the same x-position, it is assumed that the momentum remains approximately constant within this region, ensuring a more accurate subtraction.
Following the subtraction, the momentum effect is not expected to cancel completely, as the quadratic subtraction isolates the contribution of the target. This contribution, described by the Highland formula, remains inversely proportional to the momentum. Thus, the approach ensures that the subtraction process properly reflects the effect of the target while minimizing momentum-related discrepancies.
To have as much variety as possible all combinations of different target regions for one material are used in the quadratic subtraction. Each region is quadratically subtracted by the "empty" telescope to get the contribution of the target itself and by all thinner regions respectively to get the contribution of the difference in the material budget. This yields the following thicknesses:

- 70 µm Al: Region 1 - "Empty"
- 200 µm Al: Region 2 - Region 1
- 200 µm Al: Region 3 - Region 2
- 270 µm Al: Region 2 - "Empty"
- 400 µm Al: Region 3 - Region 1
- 470 µm Al: Region 3 - "Empty"

The regions are the ones indicated in Figure 4.1 and Table 4, with "Region 1" representing the thinnest region with 70 µm Al, "Region 2" being the middle region with 270 µm Al and "Region 3" the thickest with 470 µm Al. The same can similarly be achieved for the nickel targets.
For all calibration targets projections in x are shown in Figure 4.5. Before the quadratic subtraction (figure 4.5a) the distribution widths are as expected higher then afterwards (figure 4.5b) and the difference between the material budgets can be seen as a difference in the observed scattering angle distribution width θ_0. Larger material budgets have larger scattering angle distribution width θ_0. The left and right edges of each figure, where the projections fluctuate more is where side effects coming from the target holder or the sensors PCB come into play. Those regions will later be disregarded, as they would influence the measurement. For each calibration material there are four different regions, three of which are with different material thicknesses and one with an "empty" region. It is visible that the "empty" regions (the lowest blue and green lines in figure 4.5a) of both targets and the pure

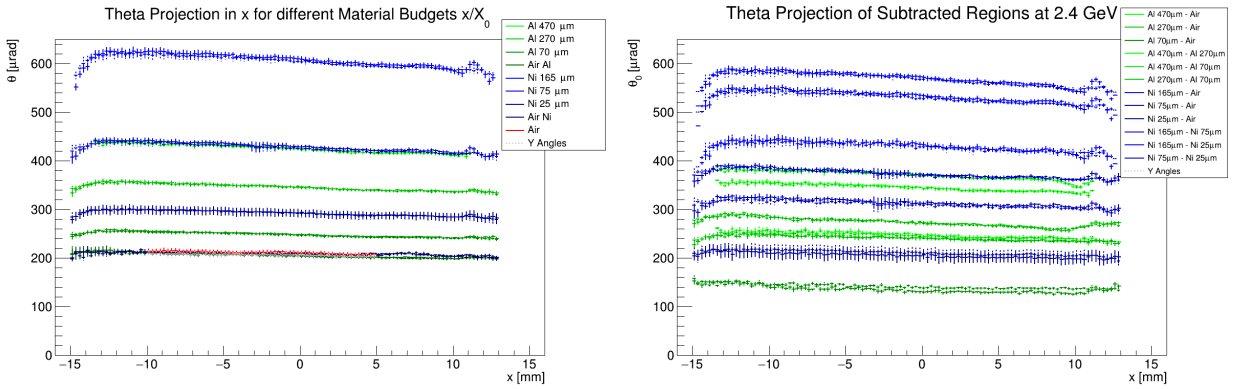

(a) Before any subtractions

(b) After quadratic subtractions

Figure 4.5: Projection in x for theta angles of the different regions of the calibration targets nickel (blue) and aluminum (green) at $E = 2.4\,\mathrm{GeV}$

"empty" measurement (red) lie very close to each other. This is expected as they all should measure the same quantity, the underlying scattering with air.

Another notable feature is the slope of each projection from left to right, which directly reflects the previously mentioned momentum gradient. According to the Highland formula (8), the scattering angle distribution width θ_0 is inversely proportional to the momentum of the incoming particles ($\theta_0 \sim 1/p$). As momentum increases from left to right, θ_0 correspondingly decreases. This highlights how the momentum gradient influences the observed distributions.

The observed slope also grows with an increasing material budget from bottom to top. This behavior can be attributed to the scaling properties of the Highland formula, where the material budget amplifies the observed difference in θ_0 caused by the momentum gradient. To quantify this, the momentum on the left edge can be defined as $p_{\text{left}} = p$ and at the right edge as $p_{\text{right}} = p + \Delta p$, where Δp is the difference in momentum. From the Highland formula, the scattering angle width is:

$$\theta_0 = f(x/X_0) \cdot \frac{1}{p}. \tag{27}$$

The difference in the scattering angle widths across the projection, $\Delta\theta_0$, is then:

$$\Delta\theta_0 = \theta_{left} - \theta_{right} \tag{28}$$

$$= \left[f(x/X_0) \cdot \frac{1}{p} \right] - \left[f(x/X_0) \cdot \frac{1}{p + \Delta p} \right] \tag{29}$$

$$= f(x/X_0) \cdot \left(\frac{1}{p} - \frac{1}{p + \Delta p} \right) \tag{30}$$

$$= f(x/X_0) \cdot \frac{\Delta p}{p \cdot (p + \Delta p)} \tag{31}$$

This demonstrates that the difference in θ_0 caused by the momentum gradient is directly proportional to the material budget x/X_0. Therefore, for larger material budgets, the variation in θ_0 due to a change in momentum becomes more pronounced. A correction for this momentum gradient will be discussed in Chapter 5.3.

4.4 Highland non-linearity factor

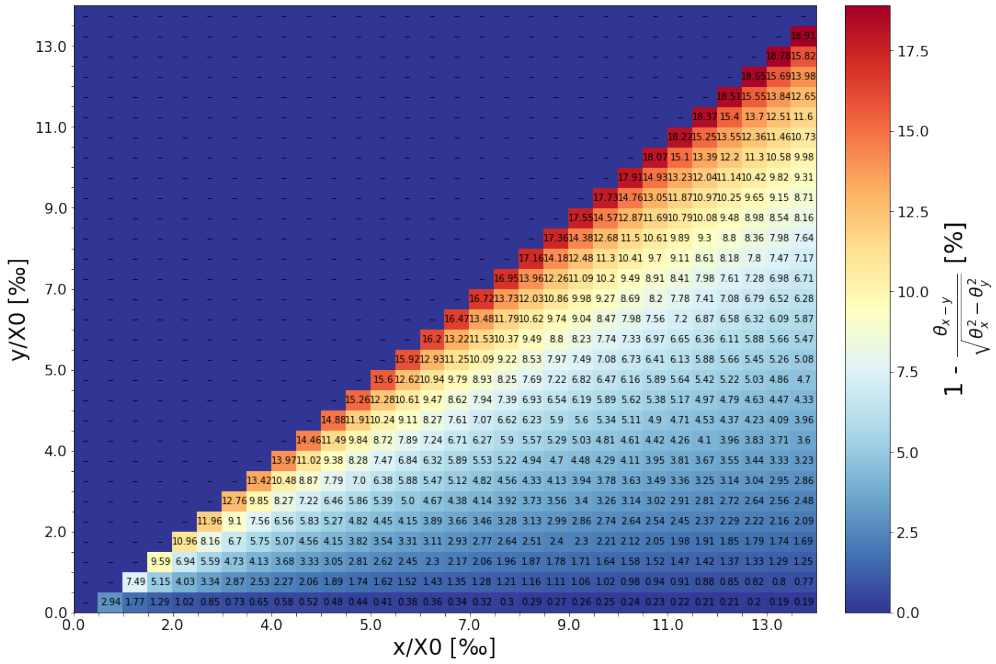

Figure 4.6: Unity subtracted scaling factor accounting for the non-linearity of the Highland formula for two different materials.

When applying quadratic subtraction, it was initially assumed that this method would effectively cancel all contributing effects, leaving only the contribution from the material budget

difference. For instance, when the standard deviation of the scattering distribution from 270 µm of aluminum is subtracted from that of 470 µm of aluminum, the result was expected to represent the contribution of the additional 200 µm of aluminum alone. Similarly, subtracting the empty telescope measurement from any other measurement should isolate the contribution of the scatterer itself.

However, this assumption does not hold true because the quadratic subtraction does not fully cancel contributions arising from the non-linearity of the Highland formula. To account for this, a correction factor is required.

Consider two material budgets $a = \hat{a}/X_0$ and $b = \hat{b}/X_0$, with $a > b$. The quadratic subtraction results in a scattering angle width $\theta_{0,a-b}$ that should ideally be equal to the calculated width for the material budget difference $c = a - b$:

$$\theta_{0,c} \stackrel{?}{=} \sqrt{\theta_{0,a}^2 - \theta_{0,b}^2} = \theta_{0,a-b}. \tag{32}$$

However, due to the non-linear dependence in the Highland formula, this equality is not exact. To see this, the Highland formula is first simplified using $\ln(x \cdot y) = \ln(x) + \ln(y)$:

$$\theta_{0,x} = \frac{13.6\,\mathrm{MeV}}{\beta cp} q \sqrt{\frac{\hat{x}}{X_0}} \cdot \left[1 + 0.038 \ln\left(\frac{\hat{x}}{X_0} \cdot \frac{q^2}{\beta^2}\right)\right] \tag{33}$$

$$= \frac{13.6\,\mathrm{MeV}}{\beta cp} q \sqrt{\frac{\hat{x}}{X_0}} \cdot \left[1 + 0.038 \ln\left(\frac{q^2}{\beta^2}\right) + 0.038 \ln\left(\frac{\hat{x}}{X_0}\right)\right] \tag{34}$$

$$= A \cdot \sqrt{x} \cdot (B + C \ln(x)), \tag{35}$$

using $A = \frac{13.6\,\mathrm{MeV}}{\beta cp} \cdot q$, $B = 1 + 0.038 \ln\left(\frac{q^2}{\beta^2}\right)$, $C = 0.038$ and $x = \hat{x}/X_0$. The scattering angle widths for material budgets a and b are then:

$$\theta_{0,a} = A \cdot \sqrt{a} \cdot (B + C \ln(a)) \quad \text{and} \quad \theta_{0,b} = A \cdot \sqrt{b} \cdot (B + C \ln(b)). \tag{36}$$

With the quadratic subtraction the resulting scattering angle distribution width is:

$$\theta_{0,a-b} = \sqrt{\theta_{0,a}^2 - \theta_{0,b}^2} = \sqrt{A^2 \cdot a \cdot (B + C \ln(a))^2 - A^2 \cdot b \cdot (B + C \ln(b))^2} \tag{37}$$

$$= A\sqrt{a \cdot (B + C \ln(a))^2 - b \cdot (B + C \ln(b))^2}. \tag{38}$$

This can be compared to the calculated scattering angle distribution width for the material budget $c = a - b$:

$$\theta_{0,c} = A \cdot \sqrt{c} \cdot (B + C \ln(c)) = A \cdot \sqrt{a - b} \cdot (B + C \ln(a - b)). \tag{39}$$

The calculated scattering distribution width based on the material budget that should come out of the quadratic subtraction c (Equation (39)) should be equal to the one calculated

with the quadratic subtraction of a and b (Equation (37)). Therefore both sides can be set equal:

$$\theta_{0,a-b} = c_{a-b}\sqrt{\theta_{0,a}^2 - \theta_{0,b}^2} \tag{40}$$

$$A \cdot \sqrt{a-b} \cdot (B + C\ln(a-b)) = c_{a-b} A \sqrt{a \cdot (B + C\ln(a))^2 - b \cdot (B + C\ln(b))^2} \tag{41}$$

$$\Rightarrow \quad c_{a-b} = \frac{\sqrt{a-b} \cdot (B + C\ln(a-b))}{\sqrt{a \cdot (B + C\ln(a))^2 - b \cdot (B + C\ln(b))^2}}. \tag{42}$$

The correction factor c_{a-b} is not generally unity and therefore must be considered in quadratic subtraction. The need for such a non-linearity correction factor was first shown in [10]. Figure 4.6 shows the correction factor c_{a-b} for different material budgets in the range of the values of this thesis ($0\,‰ < x/X_0 < 14\,‰$). It can be seen that with increasing material budget and decreasing difference between a and b the correction factor increases. Notably, c_{a-b} is independent of the particles momentum, as the factor A cancels out. It also does not depend on a scaling factor s, as this could also be absorbed in A.
Defining a momentum-independent form of the Highland formula and its uncertainty:

$$\widetilde{\theta}_0 = \sqrt{\frac{x}{X_0}}\left[1 + 0.038\ln\left(\frac{x}{X_0}\right)\right] \tag{43}$$

$$\sigma(\widetilde{\theta}_0) = \frac{1}{2}\left(\frac{x}{X_0}\right)^{-1/2} \cdot \left[1 + 0.038\ln\left(\frac{x}{X_0}\right) + 0.038\right] \cdot \sigma\left(\frac{x}{X_0}\right), \tag{44}$$

with $\sigma\left(\frac{x}{X_0}\right)$ being the uncertainty of the material budget and disregarding β as it is for high energy electrons indistinguishable from unity. With this the correction factor can be simplified:

$$c_{a-b} = \frac{\widetilde{\theta}_{a-b}}{\sqrt{\widetilde{\theta}_a^2 - \widetilde{\theta}_b^2}}, \tag{45}$$

where $\widetilde{\theta}_a$, $\widetilde{\theta}_b$ and $\widetilde{\theta}_{a-b}$ are the theoretical momentum-independent scattering angle distribution widths. The uncertainty of c_{a-b} can be calculated using Gaussian error propagation:

$$\sigma(c_{a-b}) = \left[\left(\frac{\sigma(\widetilde{\theta}_{a-b})}{\sqrt{\widetilde{\theta}_a^2 - \widetilde{\theta}_b^2}}\right)^2 + \left(\frac{\widetilde{\theta}_{a-b} \cdot \widetilde{\theta}_a \cdot \sigma(\widetilde{\theta}_a)}{\left(\widetilde{\theta}_a^2 - \widetilde{\theta}_b^2\right)^{3/2}}\right)^2 + \left(\frac{\widetilde{\theta}_{a-b} \cdot \widetilde{\theta}_b \cdot \sigma(\widetilde{\theta}_b)}{\left(\widetilde{\theta}_a^2 - \widetilde{\theta}_b^2\right)^{3/2}}\right)^2\right]^{1/2}. \tag{46}$$

Here $\sigma(\widetilde{\theta}_a)$, $\sigma(\widetilde{\theta}_b)$ and $\sigma(\widetilde{\theta}_{a-b})$ are the uncertainties of the width of the angle distribution. To apply the non-linearity correction factor in the subtraction of the scattering distribution

width of a baseline with material budget b from a measurement with material budget a, and $c = a - b$, it needs to be multiplied directly after the quadratic subtraction:

$$\theta_c = \theta_{c,before} \cdot c_{a-b} = \sqrt{\theta_a^2 - \theta_b^2} \cdot c_{a-b} \tag{47}$$

$$\sigma(\theta_c) = \sqrt{(c_{a-b} \cdot \sigma(\theta_{c,before}))^2 + (\theta_{c,before} \cdot \sigma(c_{a-b}))^2}. \tag{48}$$

Here $\theta_{c,before}$ and $\sigma(\theta_{c,before})$ are the value and uncertainty of the quadratic subtraction without any corrections applied, as introduced in section 4.3.

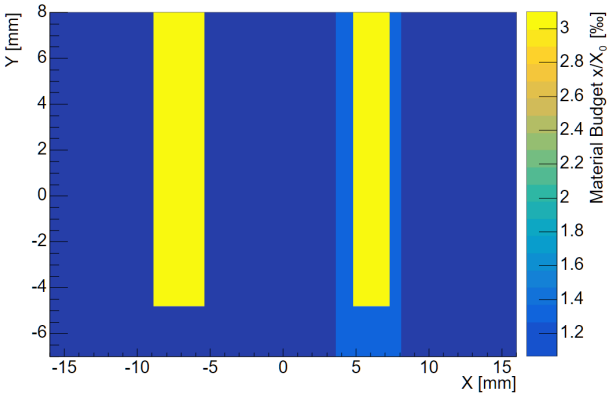

Figure 4.7: Theoretical material budget of the small sample.

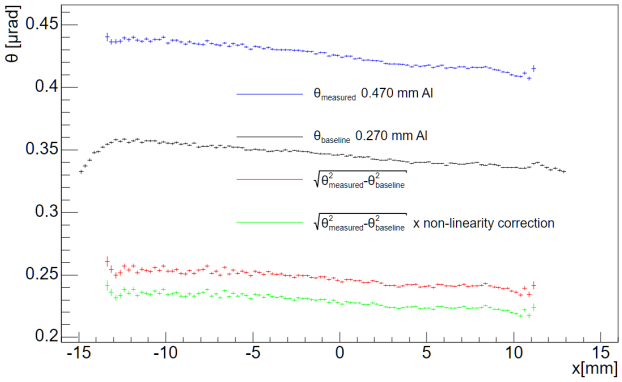

Figure 4.8: Calculation of θ for 470 µm Al minus 270 µm at $E_{set} = 2.4$ GeV.

For the calibration targets, the material budgets a and b are well-known and can be directly substituted into the equations. For measurements with an empty telescope as the baseline, the material budget for the baseline is approximated as the thickness of the target scaled by the radiation length of air.

To perform the quadratic subtraction of the empty telescope from the sample measurements, the theoretically calculated material budgets for each part of the sample are utilized. Figure 4.7 illustrates the theoretical material budget distribution for the small target, as calculated from Chapter 3.1. The placement of material budget values is done based on the two-dimensional scattering distribution. Those material budgets are then used to compute the scaling factor on a cell-by-cell basis. The resulting non-linearity scaling factor is approximately ~ 0.995 for silicon and decreases for larger material budgets.

An example of the full calculation process is shown in Figure 4.8. Starting with the originally measured scattering angle distribution width for the 470 µm aluminum target (blue), the 270 µm aluminum baseline measurement (black) is subtracted to isolate the contribution of 200 µm of aluminum. Although the figure only depicts the projection of target, the subtraction is performed cell-by-cell for the target. The projection of the resulting quadratic

subtraction is shown in red. After applying the non-linearity correction factor, the corrected curve (green) is shifted downward.

4.5 X- and Y-angle mismatch

In theory, the measured angles in the X and Y planes should be fully uncorrelated, as there is no inherent preference that would favor one over the other. However, when examining the projected ratio between the measured distribution widths of the X angles θ_X and Y angles θ_Y (see Figure 4.9), it is evident that the ratio θ_X/θ_Y is consistently greater than unity. This indicates that the X angle distributions are slightly broader than the Y angle distributions. The exact cause of this discrepancy is not yet fully understood, but it is suspected that the difference in pixel pitch of the ALPIDE sensors could be a contributing factor. The ALPIDE has a pixel pitch of 29.24 µm × 26.88 µm, which results in a better resolution along the Y axis, due to the smaller pitch. This improved resolution could lead to a narrower observed scattering angle distribution in the Y plane, causing the ratio θ_X/θ_Y to be slightly greater than one.

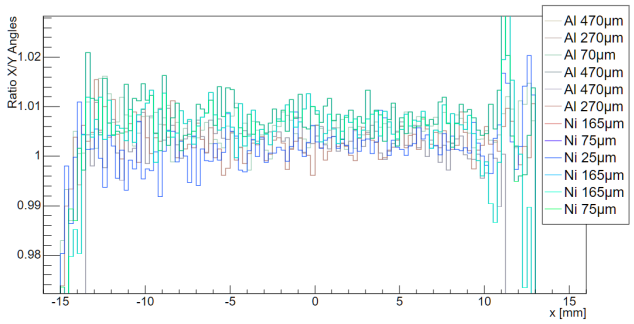

Figure 4.9: Projection of the cell-by-cell ratio of X and Y angles before any subtraction. Colors indicate different regions.

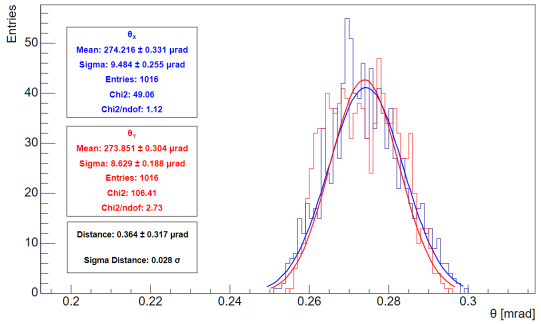

Figure 4.10: $\theta_0 = \sqrt{\theta^2_{270\,\mu m,Al} - \theta^2_{70\,\mu m,Al}}$ distribution for X (blue) and Y (red) angles.

After performing the quadratic subtraction and the non-linearity correction to isolate the scattering contribution from the baseline measurement, which also contains the intrinsic resolution of the telescope, this increased ratio is no longer observed. This outcome is expected, as the quadratic subtraction is intended to remove the effects of the telescope resolution, equalizing the observed scattering widths in the X and Y planes. Figure 4.10 shows the distributions of the measured scattering angles θ_0 for all data points, calculated as $\theta_0 = \sqrt{\theta^2_{270\,\mu m,Al} - \theta^2_{70\,\mu m,Al}}$. The two distributions are nearly identical and overlap within their respective widths. From this point onward the values obtained from the X and Y angles

will be treated equivalently and are combined on a cell-by-cell level by taking their weighted mean and uncertainty according to Equation (26).

4.6 Calibration targets and Highland

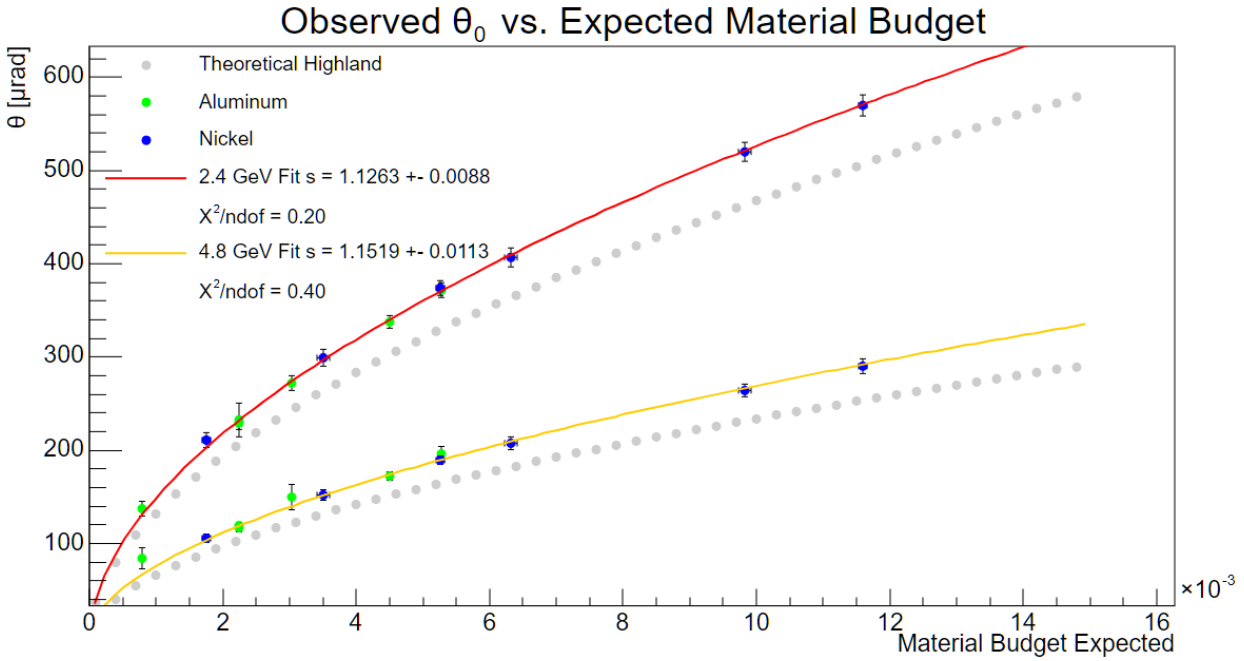

Figure 4.11: Quadratic subtracted standard deviations of scattering angle distributions for aluminum (green) and nickel (blue) compared to the Highland formula at 2.4 and 4.8 GeV.

In previous studies on material budget measurements via scattering, variations in θ_0 caused by momentum gradients were treated as systematic uncertainties [10; 11]. In respect to this analysis this would involve combining all θ_0 values within a region and assigning the standard deviation of these values as the systematic uncertainty. However, this approach fails to account for the fact that the observed θ_0 fluctuations are not random but are directly caused by an underlying momentum gradient, as seen in Figure 4.5b. Ignoring this gradient leads to an artificial inflation of the uncertainties, which compromises the precision of the analysis. Previous approaches would typically involve comparing these aggregated θ_0 values to theoretical predictions from the Highland formula, using the calibration targets with known material budget. As shown in Figure 4.11, this comparison reveals that the experimental data (green points represent values obtained from different regions of the aluminum target, while the blue circles correspond to those from the nickel target), lie systematically above the

theoretical Highland predictions (dotted lines). To resolve this discrepancy, a scaling factor is introduced to align the experimental values with the theoretical curves. For the 2.4 GeV data, the scaling factor is $s_{2.4} = (112.6 \pm 0.9)\%$ and for 4.8 GeV $s_{4.8} = (115 \pm 1)\%$. While such scaling factors have been consistently reported [11; 10], they lack a robust explanation and are often attributed to factors such as the choice of estimator, selection cuts, or particle momentum.

One plausible explanation lies in the treatment of particle momentum. The scaling factor, applied to the Highland formula, may effectively act as a momentum rescaling. The theoretical Highland curves assume nominal momenta during data acquisition, but adjusting the momenta to $p_{new} = p/s_p$, where p is the nominal momentum and s_p the scaling factor, brings the theoretical and experimental values into agreement. This adjustment corresponds to recalculated momenta of $p_{2.4} = 2.13\,\text{GeV}$ and $p_{4.8} = 4.17\,\text{GeV}$, with shifts of $\Delta p_{2.4} = -268\,\text{MeV}$ and $\Delta p_{4.8} = -633\,\text{MeV}$, respectively. This would mean that the scaling factor might only be introduced because the momentum was wrongly assumed.

Further evidence comes from the χ^2/ndof of the scaled Highland fits, which is close to zero. This suggests an overestimation of the θ_0 uncertainties, likely due to the inclusion of θ_0 variations caused by the momentum gradient. This artificial inflation comes from insufficient knowledge of the true extent of the gradient and the lack of methods to address it.

To overcome these limitations, the following sections propose a new approach to account for a possible lack of knowledge of the momentum and its momentum gradient by leveraging observations from calibration targets. This method will allow for a more precise separation of momentum-driven effects from the material budget contribution, improving the reliability of the analysis.

5 Momentum and momentum gradient

Until now, the analysis has not accounted for the momentum gradient observed in the scattering angle distribution widths, θ_0. This gradient appears as larger angles on the left side and smaller angles on the right, increasing uncertainties when calculating the mean and standard deviation of θ_0. To address this, the following chapter investigates the use of calibration target measurements to correct the momentum. Additionally, it will assess whether this calculated momentum can partially or fully explain the scaling factor.

5.1 Energy loss before target

Before addressing the problem of the momentum gradient, it is essential to first evaluate the momentum of the electrons that reach the target. Until now the momentum of the electrons at the position of the targets was assumed to be the same as the nominal momentum. This is not the case, as the particles loose some of their initial energy E_{init} before reaching the target, due to them interacting with the materials in their path, such as the surrounding air, the ALPIDEs and the scintillator. With the definition of the radiation length (Chapter 1.3) the leftover energy E of the electron can be calculated as:

$$E = E_{init} \cdot \prod_{Materials} \exp\left(-\frac{x_i}{X_{0,i}}\right) \quad \text{and} \quad \sigma(E) = E \cdot \left[\sum_{Materials} \sigma\left(\frac{x}{X_0}\right)^2\right]^{1/2} \tag{49}$$

Table 5 lists these materials, their approximate thicknesses, and the corresponding energy loss factors. The uncertainties were estimated based on measurements performed at the test beam facility. Due to the radiation loss the electrons will lose about $(4.7 \pm 0.1)\%$ of their initial energy. At a nominal energy of $E_{set} = 2.4\,\text{GeV}$, the energy of the particles at the target position is expected to be $E = (2.3 \pm 0.1)\text{GeV}$, corresponding to a reduction of $\Delta E = (112 \pm 7)\text{MeV}$. At higher nominal energies $E_{set} = 4.8\,\text{GeV}$, the expected energy at the target is $E = (4.6 \pm 0.1)\text{GeV}$, with a reduction of $\Delta E = (225 \pm 5)\text{GeV}$. This difference in the energy of the electrons at the target compared to the nominal energy is significant, but does not account for the full difference that would be needed according to the scaling factor. Therefore another method is used to calculate the momentum based on the measured θ_0.

Table 5: Estimated thicknesses of materials in front of the target

	Thickness x	Radiation Length X_0	Material Budget x/X_0	$\exp(-x/X_0)$
Sensors	$3 \times (50 \pm 0.1)\mu m$	9.365 cm	1.6 ‰	99.8 %
Scintillator	(1.4 ± 0.05)cm	42.7 cm	32.8 ‰	96.8 %
Air	(412 ± 20)cm	30 390 cm	13.5 ‰	98.7 %
			Total	(95.3 ± 0.1)%

5.2 Observed gradient

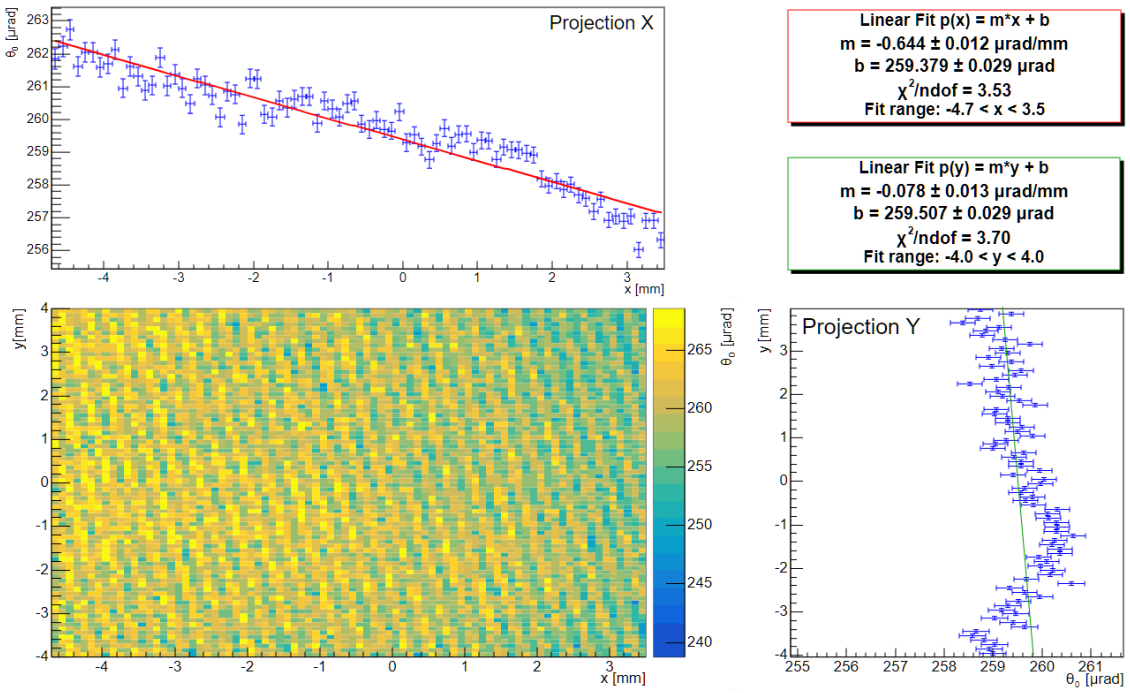

Figure 5.1: Scattering angle measured in the silicon only region of the small sample with x- and y-projections at $E_{set} = 2.4\,\text{GeV}$.

The observed scattering angle distribution width, θ_0, is inversely proportional to the particle momentum. Therefore, examining the θ_0 distribution for a uniform target provides an initial impression of the momentum distribution. Uniformity in the target ensures that any variations in θ_0 arise only from momentum changes, as all other parameters (like thickness and material budget) remain constant. The two-dimensional distribution and projections along x and y for a silicon target are shown in Figure 5.1. These values represent the directly measured θ_0 without corrections or quadratic subtractions applied.

In the x projection (top panel), a clear gradient is observed, with θ_0 decreasing from left to right. This gradient is also visible across all other targets (see Figure 4.5). In the y projection (right panel), a much smaller gradient is observed. While a gradient in y is unexpected and has not been reported by others, it cannot be cross-checked with the other calibration targets due to their limited extent in the y direction. Therefore, the y gradient is neglected and treated as a systematic uncertainty.
Since the silicon target's material budget is not expected to vary across its extent and all other effects remain constant, the observed gradient in θ_0 along x implies a momentum variation in the horizontal plane of the telescope. This momentum gradient is attributed to the beam generation process in the test beam areas at DESY.

5.3 Beam momentum determination

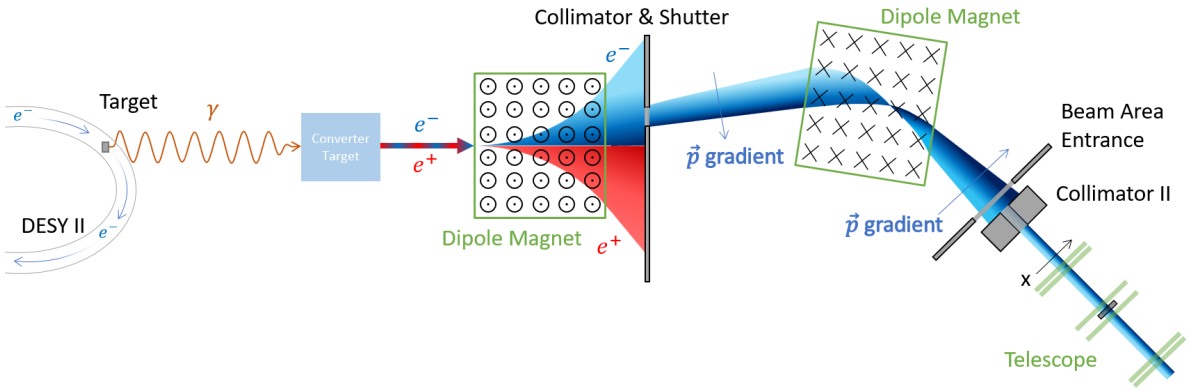

Figure 5.2: Schematic view of the beam generation for area 24 at DESY.

The beam generation process at the Test Beam (TB) area 24 at DESY is illustrated in Figure 5.2. In the synchrotron DESY II, electrons or positrons are accelerated and directed to interact with carbon fiber targets, producing a bremsstrahlung photon beam. These photons are subsequently converted into an electron-positron (e^-e^+) pair through a conversion target, such as a metal plate. A dipole magnet then separates the electrons and positrons. This process inherently introduces a momentum gradient, as lower-momentum particles experience greater deflection by the magnetic field than higher-momentum particles.
Following the separation dipole, a collimator selects particles within a specific momentum range. For the TB area 24, where the data for this thesis was collected, an additional magnet bends the beam in the opposite direction, reversing the momentum gradient. After entering the beamline, a second collimator refines the particle selection.

The momentum gradient is expected to align with the local coordinate x direction, as all deflections occur in the horizontal plane due to the vertically oriented magnetic fields of the dipole magnets. Consequently, no momentum gradient is anticipated in the y direction [28]. The observed momentum gradient, manifesting as an inverse gradient in θ_0, aligns with the expected direction. Since the material budget of the calibration target is uniform across its individual regions, the only variable that should vary, according to the Highland formula, is the momentum. Assuming the material budget of the calibration targets is known, the Highland formula can be rearranged to calculate the momentum based on the observed scattering distribution width θ_0. At these beam energies, β is approximated as unity, as changes in momentum would have an insignificant effect on β:

$$\theta_{measured} = \frac{13.6\,\mathrm{MeV}}{cp} \cdot \sqrt{\frac{x}{X_0}} \left[1 + 0.038 \ln\left(\frac{x}{X_0}\right)\right] \tag{50}$$

$$\tilde{p} = \underbrace{\frac{13.6\,\mathrm{MeV}}{c}}_{A} \cdot \underbrace{\sqrt{\frac{x}{X_0}} \left[1 + 0.038 \ln\left(\frac{x}{X_0}\right)\right]}_{\tilde{\theta}_0 :=} \cdot \frac{1}{\theta_{measured}} = A \cdot \frac{\tilde{\theta}_0}{\theta_{measured}} \tag{51}$$

$$\sigma(\tilde{p}) = \sqrt{\left(\frac{A \cdot \sigma(\tilde{\theta}_0)}{\theta_{measured}}\right)^2 + \left(\frac{A \cdot \tilde{\theta}_0}{\theta^2_{measured}} \cdot \sigma(\theta_{measured})\right)^2} \tag{52}$$

with A being a constant factor in front and $\tilde{\theta}_0$ defined as in equation (51). The momentum is calculated for each region of the calibration targets, distinguished by their unique material budgets. This calculation is performed for each cell of the two-dimensional scattering angle distribution width individually. The $\theta_{measured}$ used in this process is the quadratically subtracted and non-linearity corrected angle. Combined with the known material budget that each cell corresponds to, the momentum and its uncertainty are determined for each cell of the calibration targets.

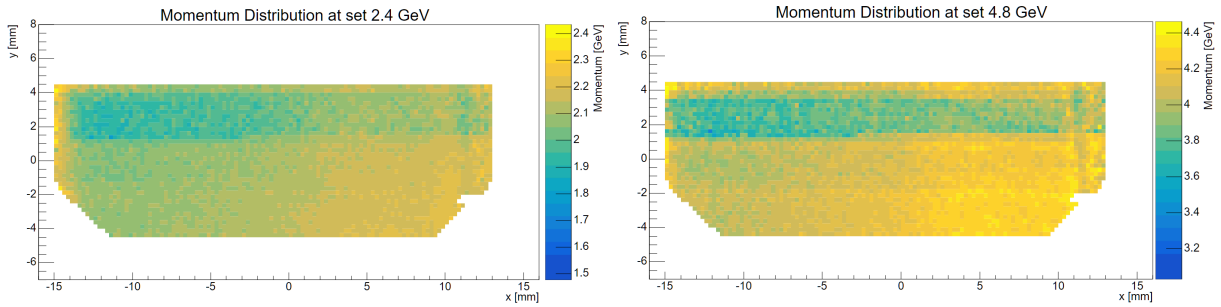

(a) $E_{set} = 2.4\,\mathrm{GeV}$ **(b)** $E_{set} = 4.8\,\mathrm{GeV}$

Figure 5.3: Averaged 2D calculated momentum distribution

As each target provides six regions with different material budgets, six two-dimensional momentum distribution maps are generated per target. Since these maps only cover small regions, they are combined into a single distribution by taking the weighted average of the momentum values for each cell, as introduced in equation (26). This procedure is repeated for both measurements, producing the averaged two-dimensional momentum distributions shown in Figure 5.3 (Figure 5.3a for $E_{set} = 2.4\,\mathrm{GeV}$ and Figure 5.3b for $E_{set} = 4.8\,\mathrm{GeV}$). These maps reveal the expected momentum behavior, increasing from left to right. However, edge effects are visible at the sensor boundaries, alongside a distinct artifact in the top region, where the apparent momentum is lower. This artifact likely arises from inaccuracies in the assumed target thicknesses, particularly in the thinnest regions. The affected areas correspond to the reported thicknesses of 70 µm (Al) and 25 µm (Ni), where deviations in thickness Δx have a stronger impact due to the relationship between the true thickness (x_{real}) and the calculated momentum:

$$\tilde{p} = \frac{A \cdot \tilde{\theta}_0(x_{real} + \Delta x)}{\theta_{measured}(x_{real})} \sim \sqrt{\frac{x_{real} + \Delta x}{x_{real}}} \tag{53}$$

For the thinnest aluminum region, the real thickness would need to be approximately 77 µm for $E_{set} = 2.4\,\mathrm{GeV}$ and 82 µm for $E_{set} = 4.8\,\mathrm{GeV}$. For nickel, the thickness would need to be around 27 µm for $E_{set} = 2.4\,\mathrm{GeV}$ and 26 µm for $E_{set} = 4.8\,\mathrm{GeV}$. While the values for nickel appear reasonable, discrepancies for aluminum vary significantly and are unexpected.

Given that the targets are composed of layered sheets of varying thicknesses, errors in estimating the thinnest layers also propagate to the calculated thicknesses of other layers. However, because momentum scales with the relative difference, the impact is less noticeable in thicker regions. Furthermore, no momentum gradient is expected along the y-direction, as noted in [11; 28].

Since the discrepancies in these regions appear to come from factors unrelated to the momentum, these regions are excluded from further analysis. Only the unaffected lower regions ($y < 1\,\mathrm{mm}$) are considered for projecting the momentum distributions.

A systematic broadening of scattering angle distributions was observed to affect each measurement. This broadening, denoted as $\theta_{\mathrm{syst.}}$, is believed to affect each target and momentum setting individually and is visible for the ITS3 samples discussed in Chapter 6.1. The broadening is thought to arise from alignment differences or sensor positioning deviations and behaves as a constant factor within each measurement configuration (same target and same energy).

At low material budgets and high energies, where the target-induced scattering angle distribution is narrower, this systematic broadening becomes relatively more significant, resulting

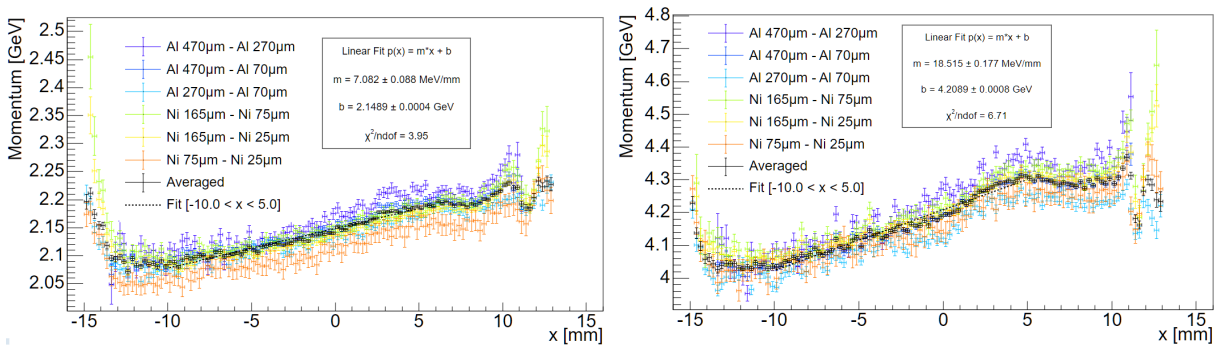

(a) $E_{set} = 2.4\,\mathrm{GeV}$ **(b)** $E_{set} = 4.8\,\mathrm{GeV}$

Figure 5.4: Projections in x of the calculated momentum for all calibration targets. The average is shown in black

in a larger relative broadening of the distribution. However, because $\theta_{\text{syst.}}$ is constant for measurements involving the same target and energy, its influence is effectively canceled out when performing a quadratic subtraction within these configurations.

In contrast, when the quadratic subtraction involves different measurements, such as between calibration targets and the "empty" telescope measurement, the systematic broadening $\theta_{\text{syst.}}$ differs between the two datasets. This discrepancy leads to a residual effect after subtraction, manifesting as an apparent increase or decrease in the resulting θ_0 and, consequently, in the inferred material budget.

Similarly, for momentum measurements, this effect persists due to the reliance on the quadratic subtraction. To prevent this, only subtractions within the same target are considered, excluding contributions from cross-measurement subtractions. For larger material budgets, the quadratic subtraction yields consistent results, as the relative contribution of $\theta_{\text{syst.}}$ becomes negligible compared to the intrinsic target scattering angle θ_0.

The x-projections of the calculated momenta for all quadratic subtractions within each target are shown in Figures 5.4a and 5.4b, corresponding to $E_{\text{set}} = 2.4\,\mathrm{GeV}$ and $E_{\text{set}} = 4.8\,\mathrm{GeV}$, respectively. The black curves represent the projection of the averaged two-dimensional momentum as a function of x, considering only regions derived from combinations within each target. The calculated momenta exhibit a consistent trend across all targets, demonstrating good agreement. A noticeable increase in momentum is observed to the right, which is quantified using a linear fit to the central region.

For $E_{set} = 2.4\,\mathrm{GeV}$, the gradient is $(7.1 \pm 0.09)\mathrm{MeV\,mm^{-1}}$, corresponding to a momentum variation of $(142 \pm 2)\mathrm{MeV}$ across the sample surface. At $E_{set} = 4.8\,\mathrm{GeV}$, the gradient is $(18.5 \pm 0.2)\mathrm{MeV\,mm^{-1}}$, corresponding to $(370 \pm 4)\mathrm{MeV}$. Previous observations only reported

a constant beam momentum spread of about (158 ± 6)MeV[28; 11], which agrees with the first result but not the second. This discrepancy suggests a deviation from the assumption of a constant momentum gradient. Since the earlier measurements were conducted in a different test beam area, these results should be compared cautiously.

5.4 Momentum calculation verification

To verify the momentum calculation, Figure 5.5 shows the projected momentum as a function of the position x, calculated using only one of the calibration targets. The procedure follows the same approach described in Chapter 5.3, but considers a single target. The results for the aluminum target are shown in blue, and for the nickel target in red.
At both $E_{\text{set}} = 2.4\,\text{GeV}$ and $E_{\text{set}} = 4.8\,\text{GeV}$, the calculated momenta agree well, with both distributions exhibiting a consistent behavior. This agreement supports the validity and reliability of the calculation method.

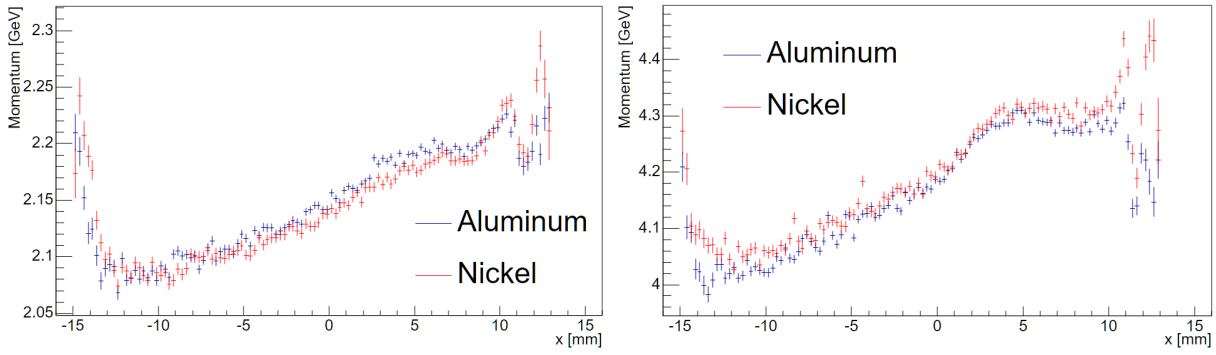

(a) $E_{set} = 2.4\,\text{GeV}$ **(b)** $E_{set} = 4.8\,\text{GeV}$

Figure 5.5: Projections in x of the momentum calculated with each calibration targets, only including quadratic subtractions within the same target.

Figure 5.6 extends the momentum calculation by including momentum calculations derived from cross-measurement regions, e.g. target subtracted by the "empty" telescope. At lower energies, such as $E_{\text{set}} = 2.4\,\text{GeV}$, the calculated momentum as a function of x remains consistent across all measurements. However, at higher energies, $E_{\text{set}} = 4.8\,\text{GeV}$, deviations arise, caused by the lower material budget of aluminum. This discrepancy supports the hypothesis that the systematic broadening $\theta_{\text{syst.}}$ impacts measurements with low material budgets and high momenta.

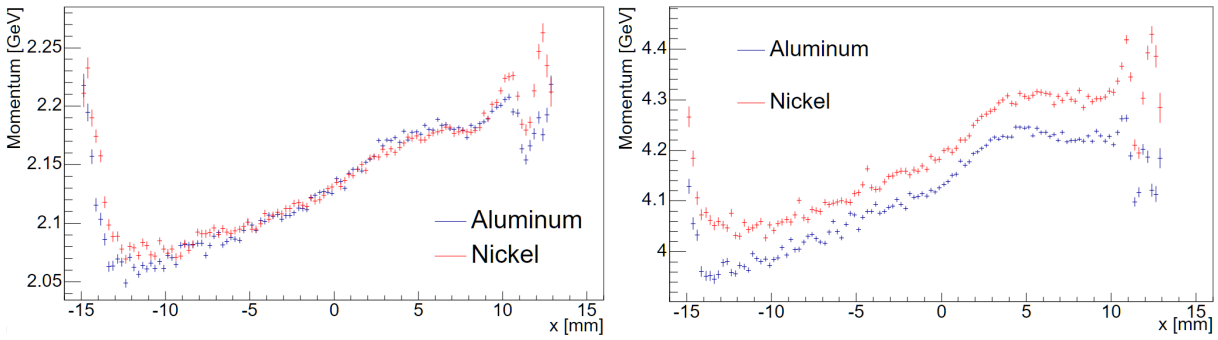

(a) $E_{set} = 2.4\,\text{GeV}$ **(b)** $E_{set} = 4.8\,\text{GeV}$

Figure 5.6: Projections in x of the momentum calculated with each calibration targets, also including cross-measurement quadratic subtraction.

5.5 Momentum gradient and telescope misplacement

By extrapolating the linear fit $p(x) = m \cdot x + b$, the position can be inferred at which the momentum is expected:

$$x = \frac{p(x) - b}{m} \quad \text{and} \quad \sigma(x) = x \cdot \sqrt{\left(\frac{\sigma(b)}{b}\right)^2 + \left(\frac{\sigma(m)}{m}\right)^2 + \left(\frac{\sigma(p)}{p}\right)^2}. \tag{54}$$

Using the expected momenta after energy loss before the target, $p = (2.3 \pm 0.1)\text{GeV}$ and $p = (4.6 \pm 0.1)\text{GeV}$ (Chapter 5.1), the calculated positions are $x_{2.3} = (20 \pm 1)\text{mm}$ and $x_{4.6} = (19.8 \pm 0.5)\text{mm}$. Both values lie outside the measurement range on the right side, indicating a possible telescope misplacement during the setup phase. This misplacement could explain the observed shift in momentum gradients.

If this hypothesis of a misplacement of the telescope is correct, it also suggests that the measurement of a constant momentum spread would not hold true [28]. Without further verification, the results cannot definitively confirm the true momentum gradient. Instead, the calculated momentum as a function of x must be treated as a convolution of the actual momentum and an unknown scaling factor, reflecting the need for additional independent momentum measurements to resolve this ambiguity.

From this point onward, the averaged apparent momentum as a function of x will be used as the reference momentum at each position x, serving as the basis for further analysis. This approach assumes that the observed momentum gradient sufficiently represents the spatial variation in the beam's momentum across the target.

5.6 Numerical inversion of Highland

Because of the nature of the Highland formula it is not possible to easily invert it to find a material budget (x/X_0) based on a given θ_0. Therefore the formula needs to be inverted numerically. To find the optimal x/X_0 for a given θ_0 the Newton-Raphson method is used [30]. It is an iterative numerical technique used to approximate solutions for any function $f(x)$. Starting from an initial guess, the method refines this estimate by leveraging the function's derivative $f'(x)$ to reach the desired target value. The updating rule is:

$$x_{new} = x_{old} - \frac{f(x_{old} - y_{wanted})}{f'(x_{old})}, \tag{55}$$

where y_{wanted} is the functions' value for which x needs to be found. With this the solution is quickly approached and the latest x_{latest} value is taken when the function at that position $f(x_{latest})$ is within a given range $|y_{wanted} - f(x_{latest})| < \epsilon$. In the case of finding the material budget $m = x/X_0$ for a given θ_0 the function in equation (55) is the Highland formula (8) with its derivative:

$$\frac{\partial\theta_0}{\partial m} = \frac{13.6\,\text{MeV}}{\beta cp} z \cdot \frac{1}{2} m^{-1/2} \cdot \left[1 + 0.038 \ln\left(m \cdot \frac{z^2}{\beta^2}\right) + 2 \cdot 0.038\right]. \tag{56}$$

The numerical integration limit is chosen to be $\epsilon = 10^{-9}$. This seems to be reasonably, as also the uncertainties of the measurement will be larger by orders of magnitude.

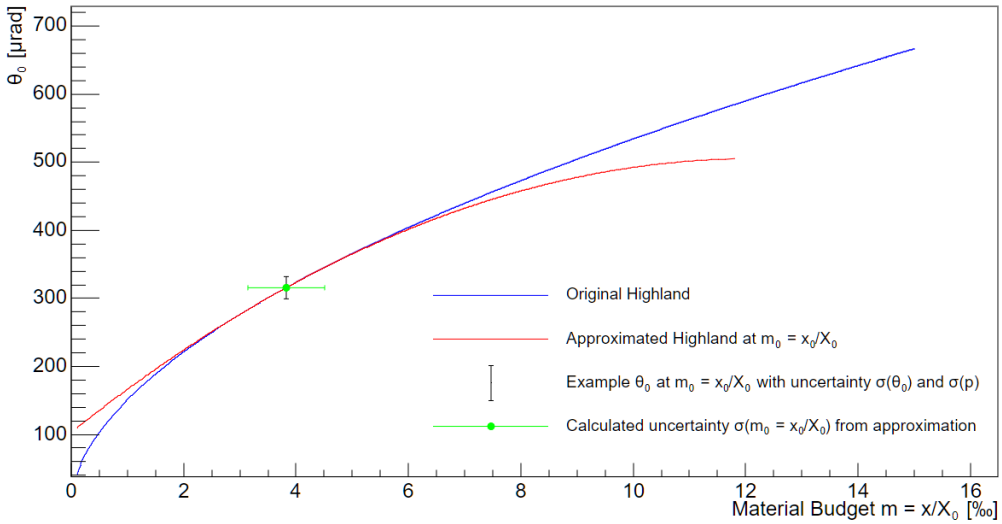

Figure 5.7: Example comparison between θ_0 calculated with the original (*blue*) and approximated (*red*) Highland at material budget x_0 ($E = 2.4\,\text{GeV}$). Also an example for the calculated uncertainty in x (*green*) based on the uncertainty in θ_0 and p (*black*) is given.

To calculate the uncertainties of $m = x/X_0$ an approximation of the Highland formula is

done with the second order Taylor series at the point of the previously calculated $m_0 = x_0/X_0$ is used [31]:

$$\theta \approx \theta_0(m_0) + \frac{\partial\theta_0(m_0)}{\partial m} \cdot (m - m_0) + \frac{1}{2}\frac{\partial^2\theta_0(m_0)}{\partial m x^2} \cdot (m - m_0)^2 \tag{57}$$

$$\approx \frac{A}{p} \cdot \left(\tilde{\theta}_0(m_0) + \partial_m\tilde{\theta}_0(m_0) \cdot (m - m_0) + \frac{1}{2}\partial_m^2\tilde{\theta}_0(m_0) \cdot (m - m_0)^2\right), \tag{58}$$

with A being the factor in front of the Highland formula and $\tilde{\theta}_0(m_0)$ being the factor and momentum independent version of the Highland formula θ_0. $\frac{\partial\tilde{\theta}_0}{\partial m}(m_0) := \partial_m\tilde{\theta}_0$ and $\frac{\partial^2\tilde{\theta}_0}{\partial m^2}(m_0) := \partial_m^2\tilde{\theta}_0$ are its first and second degree partial derivative with respect to the material budget $m = x/X_0$ respectively. All three are evaluated at the position of the previously calculated m_0 coming from the numerical inversion. By solving for m this approximation the material budget can be expressed as a function of the observed θ_0 and the momentum p:

$$\tilde{m}(\theta_0, p, m_0) \approx \frac{\sqrt{-2\tilde{\theta}_0 \cdot \partial_m^2\tilde{\theta}_0 + (\partial_m\tilde{\theta}_0)^2 + 2 \cdot \partial_m^2\tilde{\theta}_0 \cdot \frac{p}{A} \cdot \theta} - \partial_m\tilde{\theta}_0 + \partial_m^2\tilde{\theta}_0 \cdot m_0}{\partial_m^2\tilde{\theta}_0}. \tag{59}$$

The uncertainties in the observed scattering angle θ_0 and momentum p can be propagated to the material budget $m = x/X_0$ around a reference material budget m_0 using the following relation:

$$\sigma(m) = \sqrt{\left(\frac{\partial\tilde{m}}{\partial p} \cdot \sigma(p)\right)^2 + \left(\frac{\partial\tilde{m}}{\partial\theta_0} \cdot \sigma(\theta_0)\right)^2 + 2 \cdot \frac{\partial\tilde{m}}{\partial p}\frac{\partial\tilde{m}}{\partial\theta_0} \cdot \sigma(p, \theta_0)}, \tag{60}$$

with the partial derivatives of $\tilde{m}(\theta_0, p, m_0)$ being evaluated at θ_0, p and the previously calculated m_0. The total uncertainty propagation includes an additional term due to the correlation between θ_0 and p. This correlation is described by $\sigma(p, \theta_0) = \rho_{p,\theta_0}\sigma(p)\sigma(\theta_0)$, with a correlation factor $\rho_{p,\theta_0} = 1$, as they are fully correlated.

In figure 5.7, the original Highland curve is compared to the Taylor series approximation, centered at an example material budget $m_0 = x_0/X_0$. The approximation closely matches the original curve in the vicinity of m_0, as shown. The point m_0 is displayed along with its calculated uncertainty $\sigma\left(x/X_0\right)$, derived from the combined contributions of $\sigma(\theta_0)$ and $\sigma(p)$. With this approach, the material budget for a given angular distribution width θ_0 and momentum p can be determined via numerical inversion. The uncertainties in θ_0 and p are then propagated to the material budget using a Taylor series approximation, accounting for their correlation.

5.7 Verification with calibration targets

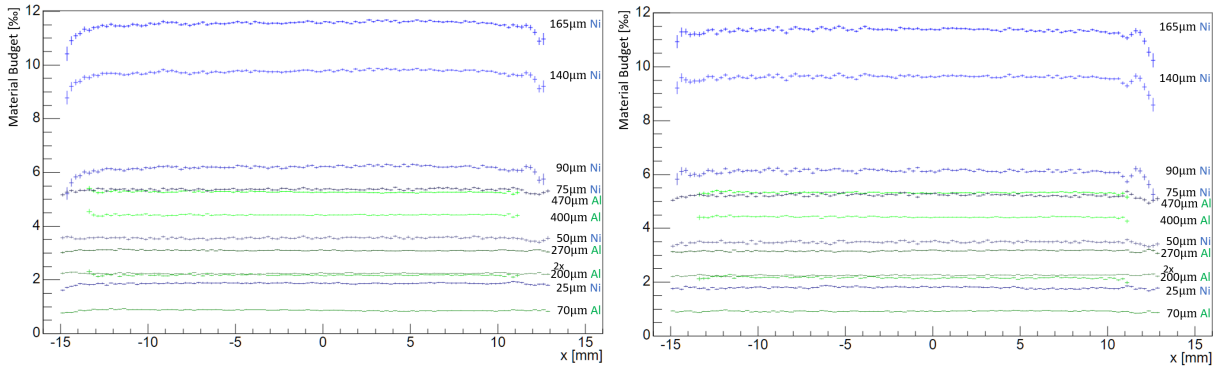

(a) $E_{set} = 2.4\,\text{GeV}$ **(b)** $E_{set} = 4.8\,\text{GeV}$

Figure 5.8: Projections in x of the calculated material budget for all calibration targets.

To verify the method of calculating the material budget from θ_0 —obtained after quadratic subtraction, non-linearity correction, and incorporating position-dependent momentum—the material budgets of the calibration targets were determined. Due to the observed systematic shift, introduced by subtracting scattering distribution widths from different measurements, the values, which require the "empty" telescope are taken from the "empty" region of each target, as shown in Figure 4.1. For the position-dependent momentum calibration, the opposite target was used: for the calculation of the material budgets of the aluminum target the momentum calibrated on the nickel targets was used and vice versa. The x-projections of the resulting material budget distributions are presented in Figures 5.8. Although the full distributions are two-dimensional maps for each target, the projections simplify quantification. The flatness of these distributions demonstrates that using the averaged momentum distribution in the Highland formula effectively cancels the observed momentum gradient, as shown for $E_{set} = 2.4\,\text{GeV}$ and $E_{set} = 4.8\,\text{GeV}$ in Figures 5.8a and 5.8b, respectively. The removal of the momentum dependence enables direct comparison of material budget values between the two energies, which agree well. The uncertainties shown represent the statistical uncertainties propagated using the previously introduced formulas. These uncertainties are minimal due to the number of measurement points in each target region along a y-row for the projection. Since each cell corresponds to an independent measurement, the uncertainty on the average reduces significantly.

The functionality of the calculated momentum is further demonstrated through its application in determining the material budget of the two samples. In this context, the observed gradient in θ_0 disappears when the material budget is calculated using the x-position-dependent

momentum. The absence of the gradient across all cases (aluminum, nickel, ITS3 and big target) indicates that the magnitude of the momentum has been accurately captured. If the momentum gradient were overestimated, applying it in the Highland formula would result in an overcorrection of the momentum's contribution. Thus, the elimination of the slopes serves as strong evidence for the validity of the momentum calculation.

Figure 5.9 compares the measured material budget for different regions of the calibration targets with their corresponding theoretical material budget values. The material budget for the aluminum regions is shown in green and red, while that for the nickel regions is displayed in blue and yellow (for $E_{set} = 2.4\,\text{GeV}$ and $E_{set} = 4.8\,\text{GeV}$ respectively). A reference line is included, indicating where the measured material budget matches the theoretical values.

The measurements are calculated by combining all measurement points within the same target region within the range $-10\,\text{mm} < x < 10\,\text{mm}$ using the weighted mean (Equation (26)). The uncertainties show only the statistical uncertainty. Due to the large number of individual measurements, the statistical uncertainty is very small.

Both the aluminum and nickel measurements show good agreement with the theoretical material budget values at both energies, confirming the accuracy of the calibration and calculation process.

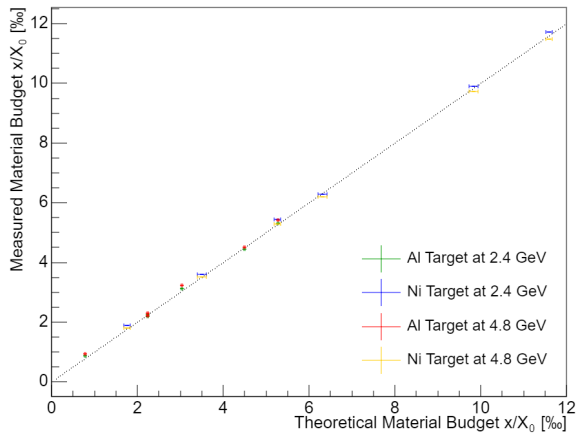

Figure 5.9: Measured material budget dependent on theoretical material budget.

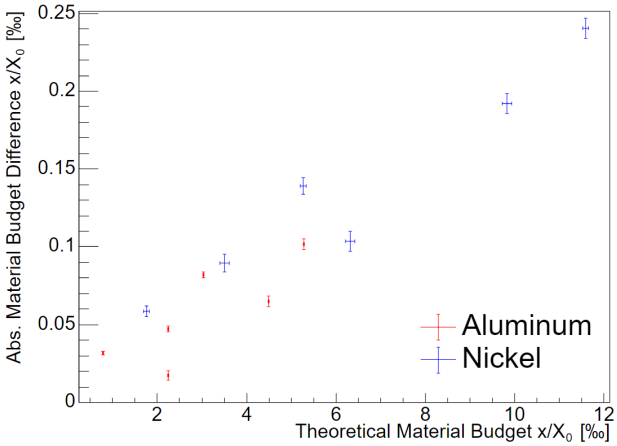

Figure 5.10: Absolute material budget difference between energies dependent on theoretical material budget.

Figure 5.10 illustrates the absolute differences in material budgets of each measurement between the two energies as a function of the theoretical material budget. The differences are smaller for regions with low material budgets and increase with larger material budgets. In the low material budget region, the differences are within 0.1 ‰ and in the higher material

budget region this rises to 0.24 ‰. These variations provide an initial indication of the systematic uncertainties in this measurement.

With an increased number of calibration measurement points in the low material budget region, relevant for the ITS3 material budget measurement ($(x/X_0) < 5\,‰$), the systematic uncertainty in this region can be reduced. This higher density of calibration points provides greater confidence in the measurement, allowing a systematic uncertainty of $\sigma_{\text{syst.}} = 0.1\,‰$ to be assumed. This approximation of the uncertainty also covers the uncertainty on the calibration targets thicknesses and therefore the momentum measurement. For larger material budgets, the systematic uncertainty increases due to fewer control points. It must be noted, that this systematic uncertainty only holds true for quadratically subtracting within the same measurement, as this cancels the systematic shift. Otherwise this systematic contribution would not cancel, leading to greater uncertainties.

Compared to earlier carbon foam measurements [10], the material budget calculation method used in this thesis reduces the systematic uncertainty. Improvements arise from creating a two-dimensional material budget map and accounting for momentum variation along x, crucial for avoiding over- or underestimation of the distribution width during quadratic subtraction. Additionally, incorporating the position-dependent momentum distribution addresses the observed gradient in θ_0, enhancing accuracy. Finally, an angular resolution-optimized setup further improves precision and minimizes systematic uncertainty.

6 Measurement of the ITS3 sample

For the ITS3 samples, the measured scattering angle distribution width θ_0 is determined by subtracting the "empty" telescope baseline measurement from the sample's θ_0 distribution. This procedure follows the same methodology as described in Section 4. Specifically, the x-projection of the "empty" measurement is used to obtain the corresponding value and its uncertainty, which are subtracted quadratically from each cell in the two-dimensional distribution. The x-projection is chosen to eliminate local fluctuations in the baseline measurement, ensuring a more uniform correction. After applying the non-linearity correction factor, derived from theoretical Highland angles, the material budget is inferred at each position using the momentum at position x, determined from the previously calculated momentum distribution, by using the numerical inversion.

The uncertainties in each cell are calculated through standard uncertainty propagation (see Equation (60)), incorporating contributions from several sources. These include the fit uncertainty on the measured scattering distribution width $\theta_{measured}$, the estimated thickness uncertainties of the sample (affecting the non-linearity correction), and the calibration targets (impacting the momentum determination).

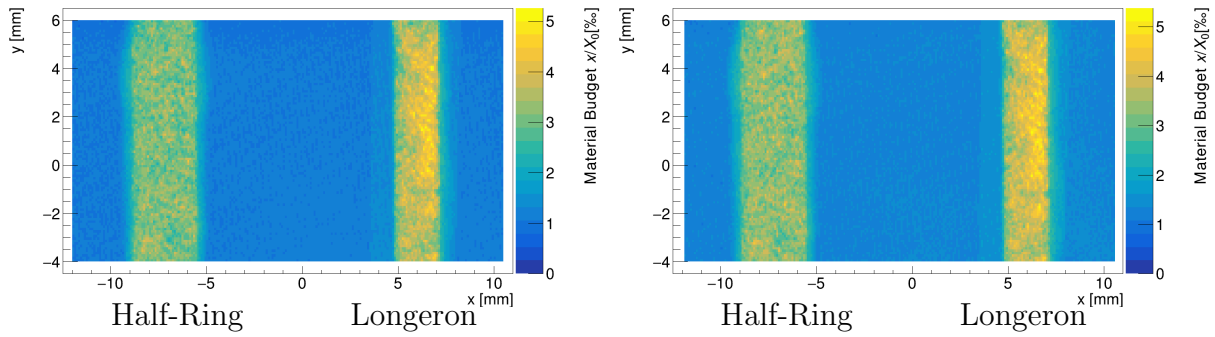

(a) $E_{set} = 2.4\,\text{GeV}$ **(b)** $E_{set} = 4.8\,\text{GeV}$

Figure 6.1: 2D material budget distribution for the ITS3 sample.

Figure 6.1 show the two-dimensional material budget distribution for the ITS3 sample at $E_{set} = 2.4\,\text{GeV}$ and $E_{set} = 4.2\,\text{GeV}$. Distinct features of the sample are clearly visible, such as the half-ring on the left and the longeron sitting on the polyimide tape on the right. Glue seepage is evident along the sides of the half-ring, consistent with the preparation process, where such seepage was anticipated. This effect is also visible in the photograph of the sample (Figure 3.1e). While the material budget of the half-ring is relatively homogeneous, individual fluctuations arise from glue seeping into the pores of the carbon foam.

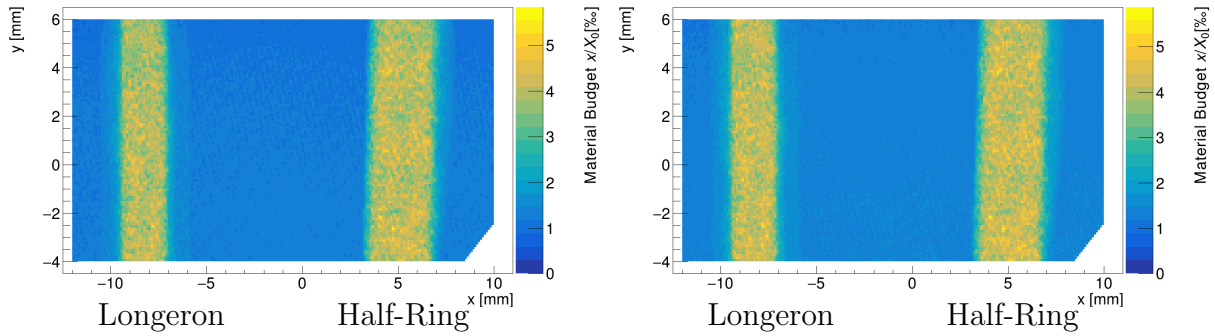

(a) $E_{set} = 2.4\,\text{GeV}$ **(b)** $E_{set} = 4.8\,\text{GeV}$

Figure 6.2: 2D material budget distribution for the big sample.

An unexpected glue hotspot is observed on the right side of the longeron, likely caused by excessive glue application during the assembly process. The background material budget corresponds to twice the material budget of a single sensor, due to the two sensors placed within the carbon foam. Only the region of interest is shown, with the holding structure and peripheral regions excluded. The distributions at both energies of the ITS3 sample appear almost identical, capturing the same fluctuations.

For the big sample (Figure 6.2), the key components are also visible, though the half-ring and longeron regions appear swapped due to the sample being flipped during insertion into the holding structure. Glue seepage is visible on the right side of the longeron, and the polyimide tape at the half-ring is clearly distinguishable. A section in the bottom-right corner is omitted due to the holding structure's presence.

When comparing the two-dimensional distributions, they exhibit similar structures, though the material budget values are slightly shifted. This can be further verified with the projections in x.

6.1 Projections of the material budget distribution

The projections of the two-dimensional material budget distributions are shown in Figure 6.3 for the ITS3 sample and Figure 6.4 for the big sample. To obtain the projections, the values in each y-column are combined using the weighted mean (Equation (26)) and its associated statistical uncertainty (blue). Additionally, the standard deviation of the measured points (gray) is presented, offering insight into the spread of values.

The standard deviation, calculated as the square root of the variance, quantifies the deviation of individual data points from the mean μ. This measure provides a clear understanding

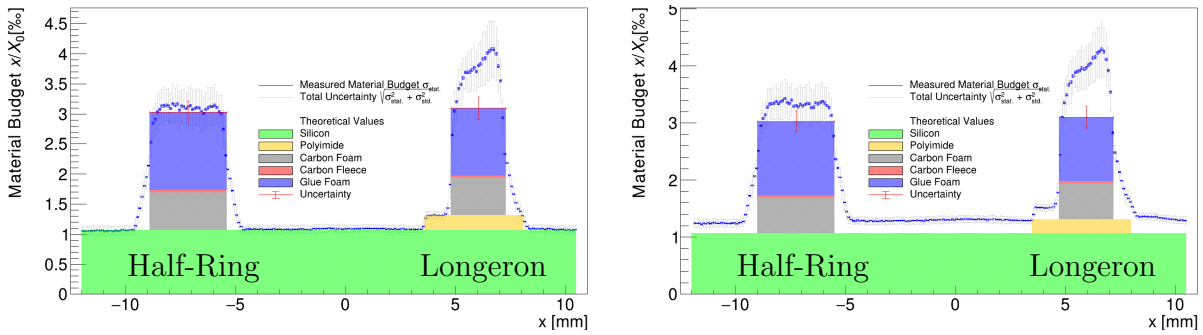

(a) $E_{set} = 2.4\,\text{GeV}$ **(b)** $E_{set} = 4.8\,\text{GeV}$

Figure 6.3: Projected material budget distribution for the ITS3 mockup sample. With $\sigma_{\text{stat.}}$ (blue) and $\sqrt{\sigma^2_{\text{stat.}} + \sigma^2_{\text{std.}}}$ (gray).

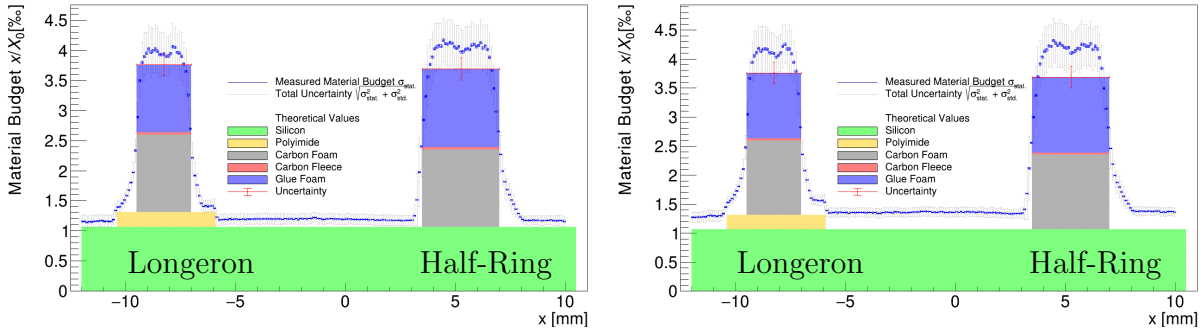

(a) $E_{set} = 2.4\,\text{GeV}$ **(b)** $E_{set} = 4.8\,\text{GeV}$

Figure 6.4: Projected material budget distribution for the big ITS3 mockup sample. With $\sigma_{\text{stat.}}$ (blue) and $\sqrt{\sigma^2_{\text{stat.}} + \sigma^2_{\text{std.}}}$ (gray).

of variability and the dispersion of values. For a normal distribution, approximately 68 % of the data lies within one standard deviation ($\pm 1\sigma_{\text{std.}}$) of the mean, as described by the formula:

$$\sigma_{\text{std.}} = \sqrt{\text{Var}(x)} = \sqrt{\frac{1}{N}\sum_{i=0}^{N}(x_i - \mu)^2} \tag{61}$$

In the projections, the previously observed gradient caused by the momentum gradient is no longer present. This is due to the implementation of the position-dependent momentum distribution, which effectively corrects for the gradient. The theoretical material budget contributions, calculated from Table 2, are indicated in different colors, with the total theoretical material budget uncertainty added on top.

For the ITS3 target (Figure 6.3), glue seepage along the sides of the half-ring is visible as a gradient on both the left and right. Additionally, the glue hotspot in the longeron region ap-

pears as a pronounced spike in the material budget. Within the uncertainties, the measured material budget for the half-ring agrees with the theoretical calculations. However, for the longeron, the observed material budget exceeds the calculated value.
In the big sample (Figure 6.4), the measured material budget for both the longeron and the half-ring regions is higher than the theoretical predictions. Glue seepage is evident on both sides of the longeron and the right side of the half-ring. Across all four projections, the contribution of the polyimide tape is clearly visible as a distinct step in the material budget, transitioning from the base contribution of the two sensors to the added contribution of the tape.

Systematic shift An overall shift in the distributions is visible, seemingly affecting each distribution by a constant offset. This appears to be a shift rather than increased fluctuations, as the standard deviation in the sensor regions does not increase but remains consistent, indicating that the values are not fluctuating more but are instead shifted by some amount.
The discrepancy in the measured sensors thickness between different energies further supports the presence of a systematic effect, as the same amount of silicon was measured at both energies. Additionally, it is unlikely that the observed shift between the ITS3 sample and the big sample originates from differences in sensor thicknesses. This strongly indicates that a systematic shift is present.
The direct cause of the observed shift in the distributions remains unknown but is suspected to come from systematic contributions $\theta_{\text{syst.}}$, such as misalignments and potential shifts in sensor positions when exchanging targets. This shift appears to manifest as a constant offset rather than increased fluctuations, suggesting that a broadening of the scattering angle distributions could be the underlying issue.
A constant broadening would be most noticeable at small material budgets and high beam energies. Under these conditions, the scattering angle distribution caused by the target is narrower, as described by the Highland formula, making the relative impact of any underlying broadening more significant. At lower energies or larger material budgets, the contribution from the scatterer itself dominates the distribution width, diminishing the relative impact of this broadening. This systematic broadening, if present for each target and energy, introduces an additional term that is not accounted for when performing quadratic subtraction between different setups (e.g., ITS3 sample subtracted by air measurement). Such a factor cannot be canceled unless the subtraction is performed within the same measurement conditions or the $\theta_{\text{syst.}}$ accidentally matches, as is most likely the case for the ITS3 measurement

at $E_{set} = 2.4\,\mathrm{GeV}$.
The issue becomes more evident when comparing the calculated momenta (Section 5.4). For larger material budgets, the scatterer's contribution dominates, making the effect of distribution broadening less noticeable. In contrast, for smaller material budgets and higher energies, the narrower distribution from the scatterer allows the systematic broadening to become more pronounced. This is reflected as a discrepancy in the calculated momenta when cross-measurement subtractions (quadratic subtraction between two regions, that are not from the same measurement) are included.
Since the systematic contribution, $\theta_{\text{syst.}}$, is assumed constant within a single measurement (same sample and energy), subtracting regions within the same measurement should cancel it. This has already been demonstrated in the momentum calculation: when regions were subtracted quadratically within the same measurement, the calculated momentum remained consistent. However, including regions obtained through quadratic subtraction across different measurements resulted in inconsistencies, particularly for small material budgets and high energies.
Further verification using the thinnest regions of the calibration targets (aluminum and nickel) is limited due to potential discrepancies between their actual and assumed thicknesses. Instead, the presence of the systematic contribution can be verified and taken out by quadratically subtracting the pure sensor regions from each sample.

6.2 Subtracting the sensors contribution

The sensors contribution is removed at the quadratic subtraction level, where the measured scattering angle θ_{measured} for each cell is quadratically subtracted by θ_{sensor}.
To determine θ_{sensor}, a region containing only the sensor's contribution is identified. The scattering angle values in this region are projected onto the x axis to reduce statistical fluctuations. A linear fit, $\hat{\theta}(x) = m \cdot x + b$, is then applied to this projection, providing an x-dependent estimate of the sensors contribution.
As explained in Chapter 4.3, θ_{measured} and θ_{sensor} must correspond to the same x position because of the momentum gradient. Any mismatch in x would lead to differences in momentum, causing inaccuracies in the subtraction due to over- or underestimation of the scattering angle distribution widths. The uncertainty in $\hat{\theta}_{\text{sensor}}(x)$ is calculated as:

$$\sigma(\hat{\theta}(x)) = \sqrt{(m \cdot \sigma(x))^2 + (x \cdot \sigma(m))^2 + (\sigma(b))}, \tag{62}$$

where $\sigma(x)$, $\sigma(m)$, and $\sigma(b)$ represent the uncertainties in x, the slope, and the intercept, respectively.

After the quadratic subtraction, a non-linearity correction based on the theoretical material budgets of the sensor region and sample is applied. Finally, the material budget for each cell is obtained through numerical inversion, with its uncertainty propagated using a Taylor expansion at the inversion point.

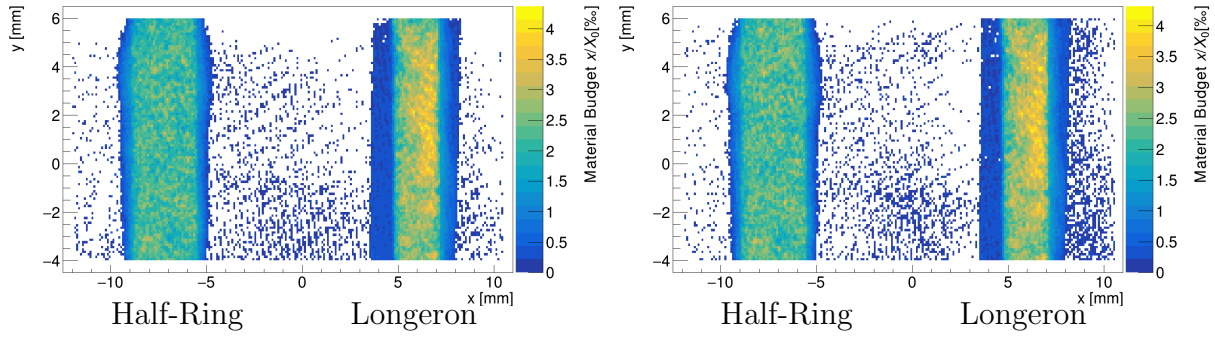

(a) $E_{set} = 2.4\,\text{GeV}$ **(b)** $E_{set} = 4.8\,\text{GeV}$

Figure 6.5: 2D material budget distribution for the ITS3 sample with the sensors contribution subtracted.

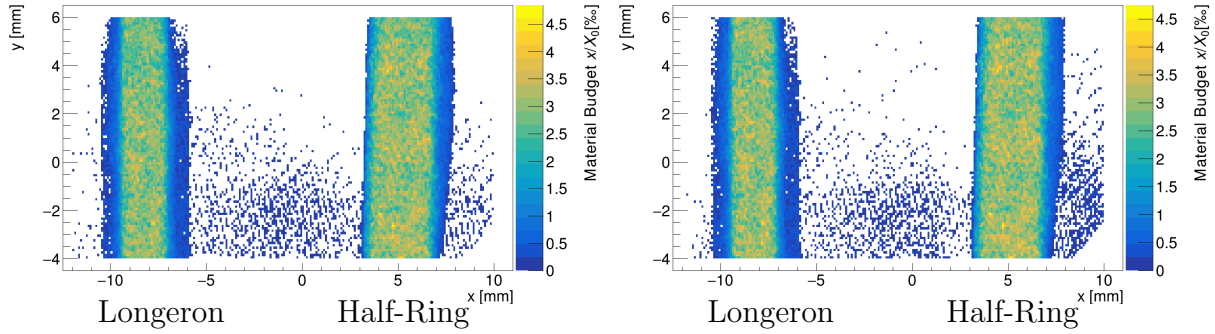

(a) $E_{set} = 2.4\,\text{GeV}$ **(b)** $E_{set} = 4.8\,\text{GeV}$

Figure 6.6: 2D material budget distribution for the big sample with the sensors contribution subtracted.

Figure 6.5 shows the two-dimensional sensor-subtracted material budget of the ITS3 sample at $E_{set} = 2.4\,\text{GeV}$ and $E_{set} = 4.2\,\text{GeV}$. Distinct contributions from the longeron and half-ring carbon foam structures are evident, with the half-ring displaying a homogeneous material budget and a hotspot observed at the longeron. Features such as the polyimide tape near the longeron on both sides and gradients near the half-ring and the right side of the longeron, likely caused by glue seepage, are also visible.

The material budget distribution at $E_{\text{set}} = 4.8\,\text{GeV}$ closely matches the $E_{\text{set}} = 2.4\,\text{GeV}$ distribution in the carbon foam regions. Similarly, the big sample (Figure 6.6) shows consistent results, demonstrating the reliability, repeatability, and precision of the measurements in capturing the same physical properties. Notably, the big sample lacks any material budget hotspot, with both the half-ring and longeron exhibiting a homogeneous material budget distribution.

Because sensor subtraction was performed using the average θ_{sensor} contribution across each y column, some small residual contributions remain due to incomplete cancellation. A slight y dependence is noticeable, particularly in the sensor-only regions, where leftover cells are more prevalent at lower y values. This effect is well described within the systematic uncertainties.

6.3 Sensor subtracted material budget projections

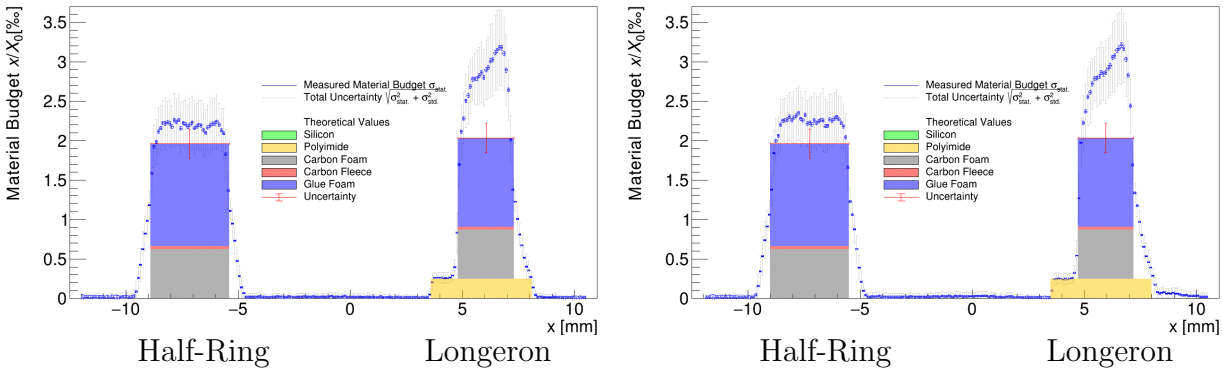

(a) $E_{set} = 2.4\,\text{GeV}$ **(b)** $E_{set} = 4.8\,\text{GeV}$

Figure 6.7: Projected material budget distribution for the ITS3 mockup sample with underlying sensor contribution subtracted. With $\sigma_{\text{stat.}}$ (blue) and $\sqrt{\sigma^2_{\text{stat.}} + \sigma^2_{\text{std.}}}$ (gray).

Figures 6.7 and 6.8 display the x-projections of the sensor-subtracted material budget distributions derived from the two-dimensional material budget distribution, with the statistical uncertainty (blue) and the standard deviation (gray) indicated.

By comparing the two energies for each target, the distributions show excellent agreement. In both targets, the systematic shift is effectively removed, and the material budget distributions exhibit consistent behavior across both energies.

In all cases, the distributions follow a similar trend as observed with the quadratic subtraction of the "empty" telescope, with the key difference being the absence of the systematic shift. This confirms the presence of a systematic effect, which can be successfully elimi-

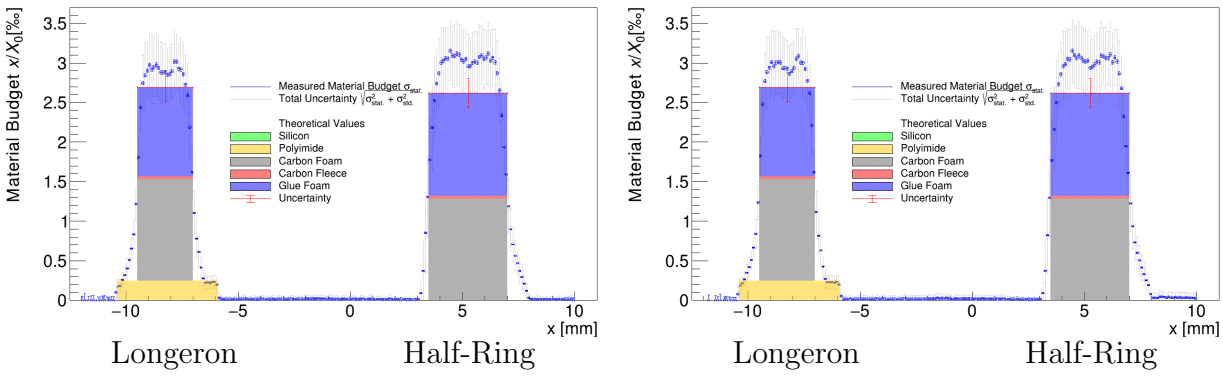

(a) $E_{set} = 2.4\,\mathrm{GeV}$ **(b)** $E_{set} = 4.8\,\mathrm{GeV}$

Figure 6.8: Projected material budget distribution for the big ITS3 mockup sample with underlying sensor contribution subtracted. With $\sigma_{\mathrm{stat.}}$ (blue) and $\sqrt{\sigma^2_{\mathrm{stat.}} + \sigma^2_{\mathrm{std.}}}$ (gray).

nated through quadratic subtraction, provided both measurements are affected by the same amount, as is the case when subtracting within the same measurement.

For the ITS3 sample (Figure 6.7), the half-ring and glue seepage are clearly visible on the left side. Glue seepage is apparent on both sides and can be confirmed by inspecting the sample photo (Figure 3.1e) and the CT scan, which highlights the seepage on the top and bottom parts (Figure 6.9). The observed material budget is slightly higher than predicted by theoretical calculations. The previously noted material budget increase and potential glue hotspot in the longeron are visible for both energies. Additionally, the step caused by the polyimide tape is visible and serves as a benchmark for evaluating the precision of the method used in this thesis.

Similarly, for the big sample (Figure 6.8), the polyimide tape step is distinct and matches the anticipated material budget. Both the half-ring and longeron measurements are slightly higher than expected, likely due to excess glue used during assembly. Glue seepage is evident as a gradient in the material budget near the edges of the carbon foam structures.

The statistical uncertainty of the measurement (blue) is particularly small due to the large number of measurement points collected across the sample in a row in y. As each individual data point contributes to refining the final result. The more measurements there are, the better the average value can be determined, helping to minimize the influence of random fluctuations.

The standard deviation combined with the statistical uncertainty (gray) highlights that the material budget in the half-ring and longeron regions fluctuates more than in areas containing only the sensors. Since the standard deviation values are smaller in the sensor regions,

this suggests that the measurement itself is not subject to significant inaccuracies. Therefore, the increased standard deviation values observed in the half-ring and longeron regions can be attributed to real fluctuations in the material budget. These fluctuations are likely caused by glue seeping into the carbon foam. The localized accumulations of glue lead to variations in the material properties, creating areas with both increased and decreased material budgets, which drive the observed fluctuations in the measured distribution.

6.4 Material budget of the components

Table 6: Measured and theoretical material budget for individual components with statistical uncertainty (first) and standard deviation (second)

Target	Energy	Half-Ring [‰]	Longeron [‰]	Polyimid Tape [‰]
ITS3	2.4	2.200 ±0.004(±0.323)	2.895 ±0.006(±0.483)	0.285 ±0.002(±0.063)
	4.8	2.243 ±0.004(±0.336)	2.908 ±0.006(±0.486)	0.265 ±0.002(±0.069)
Theoretical		2.0 ±0.2	2.0 ±0.2	
Big	2.4	3.070 ±0.005(±0.399)	2.939 ±0.005(±0.393)	0.271 ±0.003(±0.083)
	4.8	3.043 ±0.005(±0.408)	2.966 ±0.006(±0.407)	0.273 ±0.003(±0.082)
Theoretical		2.6 ±0.2	2.7 ±0.2	0.245 ±0.004

By defining polygonal regions corresponding to the half-ring, the longeron, and the polyimide tape, the material budget of these regions can be determined. Table 6 summarizes the obtained values. The uncertainties include the statistical uncertainty from propagated errors and the standard deviation (square root of the variance).
The systematic uncertainty of $\sigma_{\text{syst.}} = 0.1\,‰$ accounts for the variations seen on the calibration targets (Chapter 5.7), as well as for the observed slight y dependence seen in the sensor only contribution (Chapter 5.2). Other effects, like the uncertainty of the thickness of the calibration targets, propagate to the uncertainty on the momentum are covered with this.
For the ITS3 sample, the half-ring measurements at both energies agree within the systematic uncertainty. Both measurements agree within the systematic uncertainty with the theoretical value. For the longeron, while the measurements agree with each other, they are higher than the theoretical prediction. This discrepancy is likely due to excess glue applied during the assembly process. The estimated glue contribution is $\Delta(x/X_0)_{\text{glue}} \approx 0.9\,‰$, corresponding to an additional thickness of approximately $\Delta x_{\text{glue}} \approx 360\,\mu\text{m}$. Although this seems substantial, it is feasible given the glue application process. A CT scan (Chapter 6.5)

confirms that the observed difference is indeed caused by excessive glue. Combining the measurements at both energies yields:

$$(x/X_0)_{\text{Half-Ring}} = (2.222 \pm 0.003_{\text{stat.}} \pm 0.1_{\text{syst.}}(\pm 0.466)_{\text{std.}})\,‰ \tag{63}$$

$$(x/X_0)_{\text{Longeron}} = (2.902 \pm 0.004_{\text{stat.}} \pm 0.1_{\text{syst.}}(\pm 0.685)_{\text{std.}})\,‰ \tag{64}$$

For the big sample, the measurements of both the half-ring and longeron are consistent across both energies within the systematic uncertainty. Combining the measurements from both energies yields:

$$(x/X_0)_{\text{Big Half-Ring}} = (3.057 \pm 0.004_{\text{stat.}} \pm 0.1_{\text{syst.}}(\pm 0.571)_{\text{std.}})\,‰ \tag{65}$$

$$(x/X_0)_{\text{Big Longeron}} = (2.952 \pm 0.004_{\text{stat.}} \pm 0.1_{\text{syst.}}(\pm 0.566)_{\text{std.}})\,‰ \tag{66}$$

They deviate slightly from the theoretical values, indicating that slightly too much glue was applied during the assembly process. The difference to the half-ring, $\Delta(x/X_0)_{\text{Big Half-Ring}} \approx 0.4\,‰$, corresponds to an excess glue thickness of approximately $\Delta x_{\text{glue}} \approx 160\,\mu\text{m}$. For the longeron, the difference of $\Delta(x/X_0)_{\text{Big Longeron}} \approx 0.2\,‰$ corresponds to $\Delta x_{\text{glue}} \approx 80\,\mu\text{m}$. For all measurements, it is more reasonable to attribute the deviations from theoretical values to a misjudgment of the amount of glue applied rather than to inaccuracies in the theoretically calculated radiation lengths and material budgets. Consequently, it is not possible to determine the material budget differences due to the increased height of the carbon foam when comparing the big sample and the ITS3 sample, as the glue amount is unknown and unreliable.

The polyimide tape measurements exhibit slight variations between the ITS3 sample and the big sample, but they agree well within the standard deviation. Combining measurements at both energies for each target yields:

$$(x/X_0)_{\text{ITS3 polyimide}} = (0.275 \pm 0.001_{\text{stat.}} \pm 0.1_{\text{syst.}}(\pm 0.093)_{\text{std.}})\,‰ \tag{67}$$

$$(x/X_0)_{\text{Big polyimide}} = (0.272 \pm 0.002_{\text{stat.}} \pm 0.1_{\text{syst.}}(\pm 0.117)_{\text{std.}})\,‰ \tag{68}$$

Withing the systematic uncertainties they agree with the theoretical value. However, this needs to be treated with caution as the measured values are not significantly different from zero ($< 3\sigma$). The low fluctuation, reflected in the small standard deviations, combined with the clear visibility of polyimide in material budget distributions (2D and projections), suggests that statistical uncertainties may be overestimated. This observation might also indicate that it is indeed possible to measure the contribution of the polyimide tape, highlighting the sensitivity of the method. Further investigation into systematic uncertainties is required to validate this conclusion.

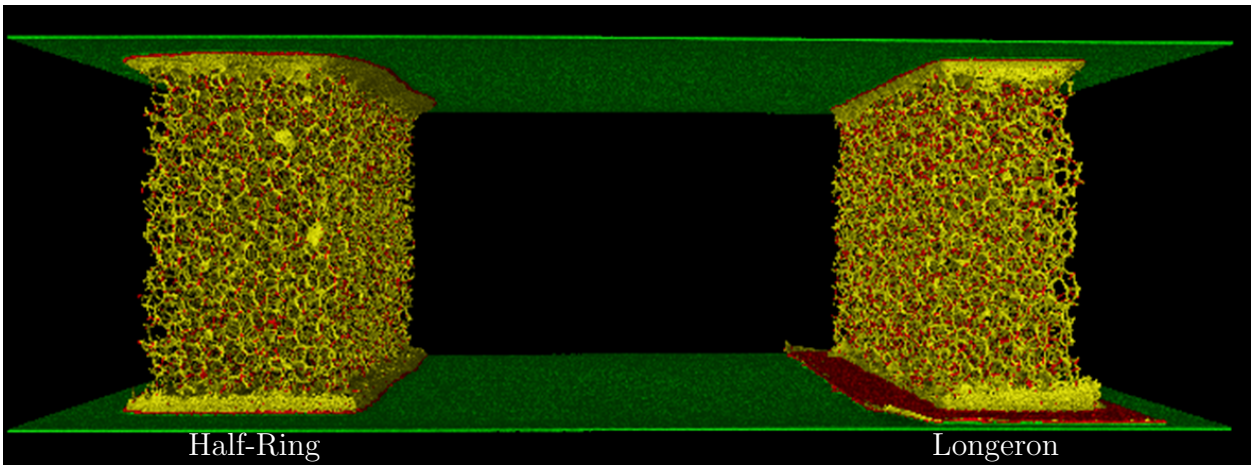

Figure 6.9: CT scan of the ITS3 sample. Different colors show different amounts of absorption.

6.5 CT scan

For an additional cross-check, a CT scan of the samples was performed at CERN. A side view of the scan is shown in Figure 6.9. Post-processing was applied to add colors, with each color representing different levels of absorption. This enables the differentiation of materials: the polyimide tape is highlighted in red, the glue appears as red and yellow, the carbon foam as yellow, and the sensors as green.

On the half-ring side, the previously observed glue seepage is clearly visible in the CT scan. In contrast, no seepage was detected on the left side of the longeron, consistent with the results of the earlier material budget analysis.

Figure 6.10 displays slices of the CT scan taken on planes parallel to the sensors, positioned just at the edge where the half-ring glue ends. These slices clearly highlight the glue's irregular penetration into the carbon foam, as seen by the bright regions. Glue presence is evident at the longeron in both cases, confirming its uneven distribution and excessive application.

The CT scan reveals the irregularity of glue penetration into the carbon foam, which appears in earlier measurements as material budget variations within the carbon foam region. It confirms observations from the material budget analysis and directly links the excess material budget in the longeron to an overestimation of the required glue.

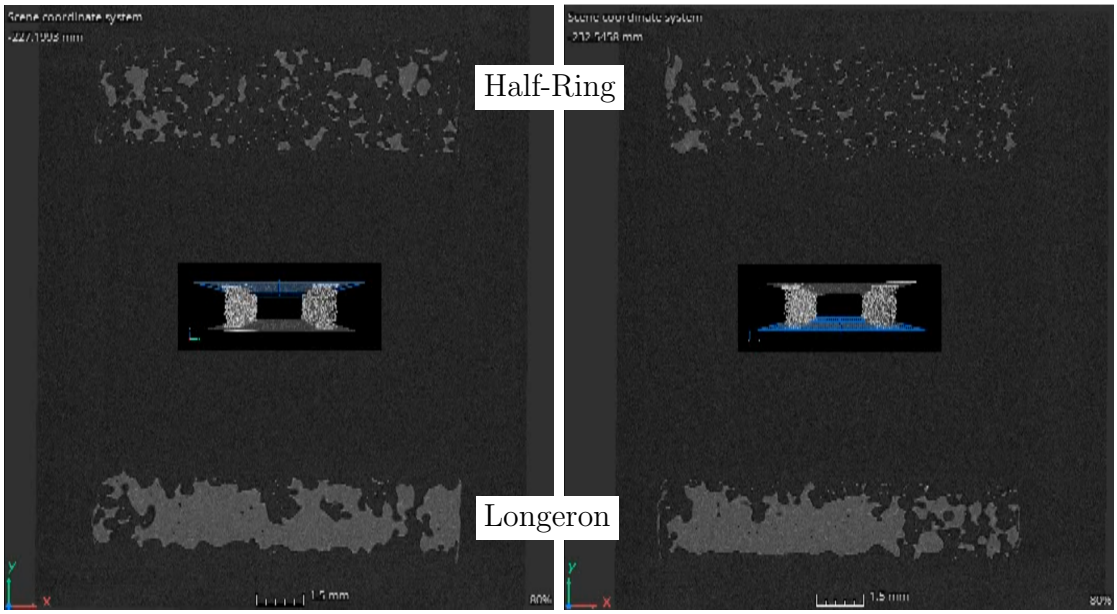

(a) Bottom **(b)** Top

Figure 6.10: CT scan slice of the ITS3 sample at different positions.

7 Conclusion and outlook

In this thesis, material budget imaging was performed on various targets, including ITS3 mockup samples, using an electron beam. The primary goal was to measure the material budgets of different ITS3 components and validate the assumed values. The ITS3, designed to replace the inner barrel of the ITS2 in the ALICE experiment, aims to reduce the material budget significantly. This reduction is achieved using carbon foam support structures, which provide stability for the wafer-scale bent sensors. To validate the expected material budgets, a mockup sample was constructed, and the material budget was measured via electron scattering.

Using a setup optimized for angular resolution, the scattering angles of electrons interacting with different targets were measured. By defining regions a two dimensional grid was created with each cell holding the scattering angle distribution of electrons scattering in that region. By fitting a Gaussian to 98 % of the distribution, the width and its uncertainty were extracted, yielding a two-dimensional map of scattering angle distribution widths. Quadratic subtraction was performed to isolate the contribution of the scatterer, and a non-linearity correction factor for the Highland formula was applied.

A beam momentum gradient, caused by the beam generation process at the DESY test beam areas, was previously treated as a systematic uncertainty. In this work, the position-dependent momentum was measured using scattering with calibration targets (aluminum and nickel), which was then used in the calculation of the material budget. This method eliminates the need for a scaling factor and accounts for the gradient observed in the scattering angle distributions. The approach proved to be robust, working effectively when performing the momentum measurement with one target and verifying it with the other.

A systematic shift, likely coming from misalignment or improper sensor placement, was consistently observed within individual measurements (same target and energy). This shift predominantly affects measurements with low material budgets or high momentum, where the relative change in the measured distribution widths is more pronounced. This arises because the target's scattering contribution diminishes in these cases. When performing quadratic subtraction between different measurements, this systematic effect does not cancel, leading to an over- or underestimation of the scattering angle distribution width and, consequently, the material budget. However, when quadratic subtraction is performed within the same measurement, the systematic effect cancels, indicating that it is measurement-dependent.

To address this, the material budget of the ITS3 samples were determined by subtracting in quadrature the underlying scattering angle distribution contributed by the silicon

sensors. This method determined the material budgets for the two carbon foam structures in the ITS3 sample: $(x/X_0)_{\text{Half-Ring}} = (2.222 \pm 0.003_{\text{stat.}} \pm 0.1_{\text{syst.}}(\pm 0.466)_{\text{std.}})\,‰$ and $(x/X_0)_{\text{Longeron}} = (2.902 \pm 0.004_{\text{stat.}} \pm 0.1_{\text{syst.}}(\pm 0.685)_{\text{std.}})\,‰$. The half-ring measurement aligned with theoretical predictions, whereas the longeron showed an increased material budget. A subsequent CT scan confirmed that this increase was due to excess glue. Observed material budget gradients were similarly attributed to glue seeping from the sides of the carbon foam structures.

For the big sample, the measurements of the longeron and half-ring carbon foam structures yielded: $(x/X_0)_{\text{Big Half-Ring}} = (3.057 \pm 0.004_{\text{stat.}} \pm 0.1_{\text{syst.}}(\pm 0.571)_{\text{std.}})\,‰$ and $(x/X_0)_{\text{Big Longeron}} = (2.952 \pm 0.004_{\text{stat.}} \pm 0.1_{\text{syst.}}(\pm 0.566)_{\text{std.}})\,‰$. Both measurements exceeded theoretical values, again attributed to glue.

The standard deviation reflects significant material budget variations within the carbon foam structures. Those are due to the glue penetrating the carbon foam unevenly, creating regions of increased and decreased material budget. Compared to earlier carbon foam measurements [10], the statistical uncertainty was reduced due to the two-dimensional mapping, which increased the number of measurement points. Nonetheless, the measurements remain dominated by the systematic uncertainties of $\sigma_{\text{syst.}} = 0.1\,‰$.

The polyimide tape could not be resolved within a significance interval of $< 3\sigma_{\text{syst.}}$. However, the large number of measurement points and their small standard deviation suggest that such a measurement should be feasible. Therefore, further investigation into the systematic uncertainties is necessary.

In the end the varying glue contribution is the main factor when it comes to the material budget of the ITS3. In the fabrication process of the mockup samples, the amount of glue used was not tightly controlled, leading to excess glue and hotspot regions. Improved glue application methods would be essential for future iterations.

The primary limitation of this method is the systematic shift observed at lower material budgets and higher momenta. This shift likely arises from misalignments and incorrect sensor placements, but further verification is needed to pinpoint its exact cause. In subsequent iterations of such samples, regions should be positioned to allow systematic effects to cancel through quadratic subtraction. Including regions with well-known material budgets in the same measurement could further calibrate the subtraction process, isolating systematic contributions.

Investigating the y-dependence of the measurement could provide new insights, as current

calibration targets do not extend significantly in the y-direction. Calibration targets spanning the full $x - y$ plane would make that investigation possible.
Using the optimized telescope geometry, as calculated with the telescope optimizer, could improve angular resolution, yielding more precise measurements. Additionally, eliminating the formula dependence through machine learning offers an exciting prospect. A neural network trained directly on raw scattering angle distributions, alongside target, telescope, beam, and material budget information, could model the data multi-dimensional. This approach may extend the method's validity and enhance understanding of the distributions.

To sum up, the material budget measurement was successful and improved earlier measurements of the carbon foam structures due to the improved telescope setup, the two dimensional material budget mapping and the position dependent momentum measurement. Nevertheless further research is needed to validate the systematic uncertainties and increase the measurements precision.

List of acronyms

ALICE A Large Ion Collider Experiment
ALPIDE ALICE Pixel Detector
CERN "Conseil Européen pour la Recherche Nucléaire"
DESY Deutsches Elektronen-Synchrotron
e^-e^+ electron-positron
GBL General Broken Lines
IB Inner Barrel
ITS Inner Tracking System
LHC Large Hadron Collider
LS Long Shutdown
MAPS Monolithic Active Pixel Sensor
MBI Material Budget Imaging
MC Monte Carlo
MCS Multiple Coulomb Scattering
ML machine learning
OB Outer Barrel
Pb–Pb lead–lead
PCB Polychlorierte Biphenyle
PID Particle Identification
QCD Quantum Chromodynamics
QGP Quark–Gluon Plasma
RVC Reticulated Vitreous Carbon
SM Standard Model of particle physics
TB Test Beam
TDR Technical Design Report
TPC Time Projection Chamber

References

[1] Mark Thomson. *Modern Particle Physics*. Cambridge University Press, 2013.

[2] ALICE collaboration. First lead-ion collisions in the LHC at record energy. 23 November, 2022. URL https://home.cern/news/news/experiments/first-lead-ion-collisions-lhc-record-energy.

[3] John W. Harris and Berndt Müller. The Search for the Quark-Gluon Plasma. *Annual Review of Nuclear and Particle Science*, 46(1):71–107, December 1996. ISSN 1545-4134. doi: 10.1146/annurev.nucl.46.1.71. URL http://dx.doi.org/10.1146/annurev.nucl.46.1.71.

[4] Luciano Musa. Letter of Intent for an ALICE ITS Upgrade in LS3. Technical report, CERN, Geneva, 2019. URL https://cds.cern.ch/record/2703140.

[5] The ALICE collaboration. Technical Design report for the ALICE Inner Tracking System 3 - ITS3 ; A bent wafer-scale monolithic pixel detector. Technical report, CERN, Geneva, 2024. URL https://cds.cern.ch/record/2890181. Co-project Manager: Magnus Mager, magnus.mager@cern.chds.

[6] S. Acharya et al. Calibration of the photon spectrometer phos of the alice experiment. *Journal of Instrumentation*, 14(05):P05025, may 2019. doi: 10.1088/1748-0221/14/05/P05025. URL https://dx.doi.org/10.1088/1748-0221/14/05/P05025.

[7] ALICE Collaboration. First measurement of λ_c^+ production down to $p_t = 0$ in pp and p-pb collisions at $\sqrt{s_{NN}} = 5.02$TeV. *Physical Review C*, 107(6), June 2023. ISSN 2469-9993. doi: 10.1103/physrevc.107.064901. URL http://dx.doi.org/10.1103/PhysRevC.107.064901.

[8] Jochen Klein. Triggering with the alice trd. *TRDs for the Third Millenium - 4th Workshop on Advanced Transition Radiation Detectors*, September 2011. URL https://pdfs.semanticscholar.org/87d7/68226b4e7c8a0cf2d634b6fb2042c1a5d27e.pdf.

[9] A. Zinchenko, G. Chabratova, V. Pismennaia, A. Vodopianov, and JINR. Development of algorithms for cluster finding and track reconstruction in the forward muon spectrometer of alice experiment. Technical report, ALICE Collaboration, 2007. URL https://cds.cern.ch/record/865586/files/p276.pdf.

[10] Bogdan Blidaru. *Bent Monolithic Active Pixel Sensors and Material Budget Imaging studies towards the ALICE ITS3 upgrade*. PhD thesis, University Heidelberg, 2024. still in work (unpublished).

[11] Jan-Hendrik Arling. *Detection and Identification of Electrons and Photons - Applications in the ATLAS Experiment, for the ATLAS ITk Detector and at the DESY II Test Beam*. Dissertation, Technical University of Dortmund, Hamburg, 2020. URL https://bib-pubdb1.desy.de/record/449581.

[12] Wolfgang Demtröder. *Experimentalphysik 3: Atome, Moleküle und Festkörper*. Springer Spektrum Berlin, Heidelberg, 2016. URL https://doi.org/10.1007/978-3-662-49094-5.

[13] Particle Data Group, R L Workman, et al. Review of Particle Physics. *Progress of Theoretical and Experimental Physics*, 2022(8):083C01, 08 2022. ISSN 2050-3911. doi: 10.1093/ptep/ptac097. URL https://doi.org/10.1093/ptep/ptac097.

[14] H. A. Bethe. Molière's theory of multiple scattering. *Phys. Rev.*, 89:1256–1266, Mar 1953. doi: 10.1103/PhysRev.89.1256. URL https://link.aps.org/doi/10.1103/PhysRev.89.1256.

[15] Virgil L. Highland. Some practical remarks on multiple scattering. *Nuclear Instruments and Methods*, 129(2):497–499, 1975. ISSN 0029-554X. doi: https://doi.org/10.1016/0029-554X(75)90743-0. URL https://www.sciencedirect.com/science/article/pii/0029554X75907430.

[16] Gerald R. Lynch and Orin I. Dahl. Approximations to multiple coulomb scattering. *Nuclear Instruments and Methods in Physics Research Section B: Beam Interactions with Materials and Atoms*, 58(1):6–10, 1991. ISSN 0168-583X. doi: https://doi.org/10.1016/0168-583X(91)95671-Y. URL https://www.sciencedirect.com/science/article/pii/0168583X9195671Y.

[17] Arturo Tauro. ALICE Schematics. General Photo, 2017. URL https://cds.cern.ch/record/2263642.

[18] A. Dainese et al. Infn what next: Ultra-relativistic heavy-ion collisions, 2016. URL https://arxiv.org/abs/1602.04120.

[19] Alice upgrades during the lhc long shutdown 2. *Journal of Instrumentation*, 19(05). ISSN 1748-0221. doi: 10.1088/1748-0221/19/05/p05062. URL http://dx.doi.org/10.1088/1748-0221/19/05/P05062.

[20] Gianluca Aglieri Rinella. The alpide pixel sensor chip for the upgrade of the alice inner tracking system. *Nuclear Instruments and Methods in Physics Research Section A: Accelerators, Spectrometers, Detectors and Associated Equipment*, 845:583–587, 2017. ISSN 0168-9002. doi: https://doi.org/10.1016/j.nima.2016.05.016. URL https://www.sciencedirect.com/science/article/pii/S0168900216303825. Proceedings of the Vienna Conference on Instrumentation 2016.

[21] F. Reidt. Upgrade of the alice its detector. *Nuclear Instruments and Methods in Physics Research Section A: Accelerators, Spectrometers, Detectors and Associated Equipment*, 1032:166632, 2022. ISSN 0168-9002. doi: https://doi.org/10.1016/j.nima.2022.166632. URL https://www.sciencedirect.com/science/article/pii/S0168900222002042.

[22] Felix Reidt. Alice its2 - a monolithic active pixel sensor based inner tracking system for alice. *Detector Seminar*, 2022. URL https://indi.to/vg52j.

[23] Expression of Interest for an ALICE ITS Upgrade in LS3. 2018. URL https://cds.cern.ch/record/2644611.

[24] National Institute of Standards and MD 20899 USA Technology; U.S. Department of Commerce; 100 Bureau Drive; Gaithersburg. Composition of KAPTON POLYIMIDE FILM — physics.nist.gov. https://physics.nist.gov/cgi-bin/Star/compos.pl?matno=179. [Accessed 09-08-2024].

[25] Dr Anthony Affolder. Discussion of material calculations. *Staves General Meeting*, 2011. URL https://indi.to/2ZNt7.

[26] HUNTSMAN. Technical Datasheet - Araldite® 2011 Structural Adhesive. URL https://www.freemansupply.com/datasheets/Araldite/2011.pdf.

[27] S. Spannagel and H. Jansen. GBL Track Resolution Calculator v2.0, 2016. doi: doi: 10.5281/zenodo.48795.

[28] R. Diener, J. Dreyling-Eschweiler, H. Ehrlichmann, I.M. Gregor, U. Kötz, U. Krämer, N. Meyners, N. Potylitsina-Kube, A. Schütz, P. Schütze, and M. Stanitzki. The desy ii test beam facility. *Nuclear Instruments and Methods in Physics Research Section A:*

Accelerators, Spectrometers, Detectors and Associated Equipment, 922:265–286, 2019. ISSN 0168-9002. doi: https://doi.org/10.1016/j.nima.2018.11.133. URL https://www.sciencedirect.com/science/article/pii/S0168900218317868.

[29] D. Dannheim, K. Dort, L. Huth, D. Hynds, I. Kremastiotis, J. Kröger, M. Munker, F. Pitters, P. Schütze, S. Spannagel, T. Vanat, and M. Williams. Corryvreckan: a modular 4d track reconstruction and analysis software for test beam data. *Journal of Instrumentation*, 16(03):P03008, mar 2021. doi: 10.1088/1748-0221/16/03/P03008. URL https://dx.doi.org/10.1088/1748-0221/16/03/P03008.

[30] A. Galántai. The theory of newton's method. *Journal of Computational and Applied Mathematics*, 124(1):25–44, 2000. ISSN 0377-0427. doi: https://doi.org/10.1016/S0377-0427(00)00435-0. URL https://www.sciencedirect.com/science/article/pii/S0377042700004350. Numerical Analysis 2000. Vol. IV: Optimization and Nonlinear Equations.

[31] Norbert Steinmetz. *Eindimensionale Differentialrechnung*, pages 97–127. Springer Berlin Heidelberg, Berlin, Heidelberg, 2024. ISBN 978-3-662-68086-5. doi: 10.1007/978-3-662-68086-5_4. URL https://doi.org/10.1007/978-3-662-68086-5_4.

Declaration of Authorship

Ich versichere, dass ich diese Arbeit selbstständig verfasst und keine anderen als die angegebenen Quellen und Hilfsmittel benutzt habe.

Heidelberg, den 01.12.2024,